공학박사학위논문

Dynamics of particulate suspensions in complex flow: vortex formation, channel clogging, and agglomerate breakup

복잡 유동장에서의 입자 현탁액의 거동: 와류 형성, 유로 막힘, 응집 파괴

2018년 2월

서울대학교 대학원

화학생물공학부

김 영 석

복잡 유동장에서의 입자 현탁액의 거동: 와류 형성, 유로 막힘, 응집 파괴

Dynamics of particulate suspensions in complex flow: vortex formation, channel clogging, and agglomerate breakup

지도교수 이 승 종

이 논문을 공학박사 학위논문으로 제출함

2018년 2월

서울대학교 대학원

화학생물공학부

김 영 석

김영석의 박사학위논문을 인준함

2017년 12월

위 원 장_____(인)

부위원장_____(인)

위 원_____(인)

위 원_____(인)

위 원_____(인)

ABSTRACT

Dynamics of particulate suspensions in complex flow: vortex formation, channel clogging, and agglomerate breakup

Kim, Youngseok

School of Chemical and Biological Engineering

The Graduate School

Seoul National University

In this thesis, the dynamics of particulate suspensions in complex flow, such as vortex formation, channel clogging, and agglomerate breakup, was studied. Three main goals have been pursued in this thesis.

First, the effect of silica particles in poly(ethylene oxide) (PEO) solutions on both rheological properties and vortex dynamics in micro contraction channel flow was investigated. Although the materials used in industry are not merely polymeric solutions or melts but also suspensions consisting of particles as well as polymers, the researches on the interaction between particle-polymer and their vortex behaviors inside the contraction are rare. The effect of silica particle was

demonstrated by comparing between PEO solutions and silica/PEO suspensions. The addition of 1.0 wt% silica particles caused the decrease in vortex size and delayed the formation of lip vortex and the proceeding to corner vortex. Then, as the silica concentration increased, the vortex size increased and the flow rate, at which the lip vortex and corner vortex formed, decreased. The vortex behavior inside micro contraction channel was related to the storage modulus than viscosity. The storage modulus also decreased at first and then increased with silica concentration like the vortex size. The decrease in both the vortex size and the storage modulus was arisen from the adsorption of polymers onto the silica particles. Even though 1.0wt% silica particles were added, the storage modulus decreased because the amount of free polymer in the medium significantly decreased. Then, the storage modulus increased because the amount of free polymer was kept nearly constant and the silica concentration increased. The same tendency was observed when the suspension was compensated with the additional polymers corresponding to the amount of adsorbed polymer.

In the second part of the study, the clogging mechanism of poly(styrene) particles in the flow through a single micro-pore was investigated. Together with the microscopic observation, the pressure drop was also measured. The pressure drop fluctuated according to the amount of particles deposited inside the channel. When the particles deposited and blocked the channel, the channel was clogged and the pressure drop increased sharply. During the clogging process, the particles were often detached by the flow, and interesting behaviors, such as “rolling” and “stick and detach”, were found to be the key factors that determine

whether the clogging completely occurs or not. Above a certain flow rate, the channel was not clogged and the pressure drop did not increase further. The particles deposited in the upstream had an influence on the flow path. When the particles were deposited in the upstream, the flow detoured and the vortex was formed. The effect of viscosity was examined by controlling the concentration of glycerol solution. As the viscosity and flow rate increased, the shear stress applied to the particles became larger and it was more difficult for the particles to get accumulated. When the shear stress was high enough, the particles could not withstand the flow and the channel was not clogged.

As the last part of the thesis, the deformation and breakup of a single agglomerate exposed to purely planar extensional flow in a cross channel were experimentally observed and investigated. Aggregation was generated by applying shear with destabilized poly(styrene) particles, and the fractal dimension, df, of the agglomerate was 2.25. The aggregation focused on the center of the channel by the sheath flow was rotated while approaching the stagnant point. Then, the aspect ratio increased as it was deformed close to the stagnant point. The probability of breakup and the fragment distribution were dependent upon the viscosity and flow rate, and were superimposed on a master curve as a function of the applied stress. Also, with the increase in stress, the projected area of the fragment which was split by the flow decreased with the power-law relationship and the exponent was in good agreement with the model prediction.

This work provides an insight on the effect of the interaction between

polymer and particle on the rheological properties and flow field, and it is thought to be helpful for designing various particle suspensions. It is also expected that the mechanism of agglomerate formation and breakup in the flow field will contribute to the control of the size of agglomerate required in many processes.

Keywords: particulate suspension, adsorption, vortex, clogging mechanism, aggregation, agglomerate, breakup

Student Number: 2013-30280

CONTENTS

ABSTRACT……i

CONTENTS……...v

LIST OF FIGUES……....viii

LIST OF TABLES…….…...xii

1. Introduction……...1

1.1 General introduction……2

1.2 Outline of the thesis…….……8

2. Experimental section……...10

2.1 Channel fabrication……...11

2.2 Observation system……...11

3. Effect of silica particles on vortex dynamics of poly(ethylene) oxide solutions……14

3.1 Experimental……..…15

3.1.1 Materials…….……..15

3.1.2 Channel geometry…….……19

3.1.3 Rheological measurements…….……..21

3.1.4 Dimensionless numbers…….……...21

3.2 Behavior of PEO solution…….……22

3.3 Behavior of PEO/silica suspension……..…….26

3.3.1 Vortex development…….……26

3.3.2 Effect of viscoelasticity…….30

3.4 Adsorption of polymer…….…….33

4. Clogging mechanism in contraction channel flow…….42

4.1 Experimental…….……43

4.1.1 Materials…….…..43

4.1.2 Channel geometry…….……44

4.1.3 Differential pressure drop measurement……...46

4.1.4 Operation conditions…….49

4.2 Clogging mechanism and pressure drop……51

4.3 Effect of shear stress on pressure drop and clogging..62

5. Agglomerate breakup under extensional flow……..…69

5.1 Experimental……70

5.1.1 Materials……...70

5.1.2 Channel geometry……73

5.1.3 Flow characterization……75

5.1.4 Image processing……78

5.2 Behavior of a single agglomerate……..….80

5.3 Probability of agglomerate breakup……..…..86

5.4 Fragment distribution…….……...88

5.5 Master curves…….……...98

5.6 Model prediction……101

6.

Summary……103

References……..109

국문 초록……..120

LIST OF FIGURES

Fig. 2.1 Observation system. Contraction or cross geometries were used. According to channels, the number of inlets and outlets is different and it is dealt with in each section……..13

Fig. 3.1 SEM image of the synthesized silica particles (average diameter = 260 nm, standard deviation =11.7 nm)……..16

Fig. 3.2 Zeta potential of the synthesized silica particles (error bars included). The dotted line is a simple guide line…….16

Fig. 3.3 Schematic of the 4:1 contraction channel: W_u = upstream width of the channel, W_d = downstream width, h = channel height…20

Fig. 3.4 Vortex development of PEO solutions as a function of the flow rate. The images are for PEO concentration of 1.0 wt%: (a) Newtonian-like flow at Q=0.2 ml/hr, (b) lip vortex at Q=0.3 ml/hr, and (c) corner vortex at Q=0.7 ml/hr……..25

Fig. 3.5 (a) Vortex size of PEO/silica suspensions as a function of Weissenberg number. (b) Normalized vortex size of the suspension relative to the vortex size of the PEO solution. The PEO concentration was 1.0 wt% and silica concentration varied from 0 to 8.0 wt%.....29

Fig. 3.6 Rheological properties of PEO/silica suspensions: (a) shear viscosity as a function of shear rate, (b) storage modulus (G') and relaxation time (λ) as a function of silica concentration. The PEO concentration was 1.0 wt% and the silica concentration was varied from 0.0 to 8.0 wt%. Error bars are included in (b)……32

Fig. 3.7 Rheological properties of PEO/silica suspensions: (a) shear viscosity and (b) storage modulus……37

Fig. 3.8 Vortex size of PEO0.6, PEO0.6_S1.0, and PEO0.85_S1.0 as a function of flow rate……...…..……39

Fig. 4.1 (a) A detailed view of the 4 to 1 contraction channel; W_u = upstream width of the channel, W_d = downstream width, h = channel height. (b) Schematic of a channel and visualization system. Upstream and downstream length were 10, 15 mm, respectively. ⓟ represents a pressure sensor……45

Fig. 4.2 (a) Differential pressure drop of glycerol solutions without PS particles. (b) The hydraulic resistance of glycerol suspensions with flow rate. The unit of flow rate is m^3/s. For convenience, the flow rate in ml/hr unit is also given on the upper x-axis (vertical dotted

lines)……...……48

Fig. 4.3 (a) The normalized pressure drop of Gly70PS with time. The flow rate was 0.3 ml/hr. (b) Snapshots of the contraction part. (1) to (6) in figure (a) roughly show the time of snapshots in figure (b)…….55

Fig. 4.4 (a) The normalized pressure drop of Gly70PS with time, and (b) the snapshots of the channel at the flow rate 1.0 ml/hr…….58

Fig. 4.5 Snapshots of Gly60PS at the flow rate of 1.0 ml/hr…….61

Fig. 4.6 (a) Differential pressure drop of Gly70 at various flow rates. (b) Normalized pressure drop versus normalized time…….63

Fig. 4.7 Normalized clogging pressure versus shear stress of Gly60PS, Gly70PS and Gly80PS……...……65

Fig. 5.1 The projected area versus the perimeter of the agglomerates. The slop from regression was 1.38…….72

Fig. 5.2 (a) Top view of a channel. (b) Cross region. (c) Joint region. (d) Schematics of observation system.……..74

Fig. 5.3 Flow field according to the sheath flow when the main flow rate was 1.0 ml/hr. The sheath flows were (a) 1.0, (b) 3.0, and

(c) 5.0 ml/hr……..76

Fig. 5.4 Extensional rate with various main flow rate……77

Fig. 5.5 Image process. (a) Original image. (b) Background image. (c) Image after removing the background. (d) Image after sharpening and adjusting. (e) Binary image. In the figure, the projected area and the perimeter of a target agglomerate were measure by using Image J……79

Fig. 5.6 Case for no breakup. The concentration of glycerol was 50 wt.% and the flow rate was 2.0 ml/hr. (a) Overlaid image. The agglomerate came into the cross region from upper side and left for the left. The numbers in figure indicate specific time at corresponding positions: 1 at 1.0, 2 at 6.5, 3 at 24.5, and 4 at 44 ms. (b) Projected area. (c) Aspect ratio. (d) Angle with time…82

Fig. 5.7 Case for breakup. The concentration of glycerol was 70 wt.% and the main flow rate was 1.5 ml/hr. (a) Images for the process of agglomerate breakup: 1 at 5.5, 2 at 32, 3 at 34.5, 4 at 40, and 5 at 48 ms. (b) Projected area. The vertical dotted lines represent the time when the agglomerate was broken up. The breakup times were 33, 36, and 45 ms, respectively. (c) Aspect ratio and angle before the

breakup…….....85

Fig. 5.8 Probability of breakup with the flow rate of samples……...87

Fig. 5.9 Fragment distribution of (a) Gly50PS, (b) Gly60PS, and (c) Gly70PS……..90

Fig. 5.10 (a) Fragment distribution of Gly70PS with the flow rate of 1.0 and 2.5 ml/hr. (b) Average fragment fraction of samples for flow conditions……93

Fig. 5.11 Number of fragments of (a) Gly50PS, (b) Gly60PS, and (c) Gly70PS……..95

Fig. 5.12 (a) Number of fragments of Gly70PS with the flow rate of 1.0 and 2.5 ml/hr. (b) Average number of fragments of samples for flow conditions……97

Fig. 5.13 (a) Probability of breakup, (b) mean fragment area, and (c) mean number of fragment with stress……100

Fig. 5.14 Mean projected area of fragments versus stress……102

LIST OF TABLES

Table 3.1 Sample names, concentrations, rheological properties and the adsorption of polymer per unit area. η_0 is the zero-shear viscosity, G' is the storage modulus at a frequency of 10 rad/s, λ denotes the characteristic relaxation time (measured by CaBER) and Γ is the adsorption of polymer per unit area (measured by zeta-potential & particle size analyzer ELS-Z)……..18

Table 4.1 The viscosity and shear stress at each flow rate of glycerol solutions. The shear stress is the product of the shear rate (in the parenthesis) and shear viscosity in Pa unit. Flow conditions that did not cause clogging are marked with grey boxes……50

Chapter 1. Introduction

1. Introduction

1.1 General introduction

Flow in contraction geometry

The flows inside contraction geometries have long been studied and have attracted attention due to their industrial importance and range of potential applications [1-7]. These flows have been utilized as benchmarks both in experiments and in computational rheology. There have been many studies on the flows of viscoelastic fluids due to notable features they show, such as divergent flow [8-10], elastic lip vortex [2, 4, 11], and extra pressure drop [11], none of which appear in Newtonian fluids.

While these features originate from the elasticity of the fluid, it is difficult to study the effect of fluid elasticity because high deformation rates are not easily realizable in macro-scale channels larger than a few millimeters employed in previous studies [2, 4, 7]. On the other hand, in micro-fabricated devices, strong viscoelastic effect can be observed even with dilute polymer solutions because a high rate of deformation can be achieved [9-14]. Moreover, when the flow rate is increased to obtain high Weissenberg number in a macro-channel, both the effect of elasticity and the Reynolds number increase, indicating that the inertial effect cannot be neglected. In contrast, the effect of fluid elasticity can easily be studied with a micro-channel because a high Weissenberg number can be obtained while keeping the Reynolds number low enough due to the small length scale [9, 11, 12].

The contraction geometry and the properties of the fluid affect the flow patterns. There have been a few studies on the effect of fluid elasticity and the contraction ratio [2, 4-6]. One study investigated various flow patterns inside micro-fabricated 4:1 contraction channels [15]. In that report, an initially Newtonian-like flow passed through various sequences and developed into the vortex growth regime, in which the corner vortex grew with an increase in the Weissenberg number. Diverse flow patterns were observed depending on the fluid viscoelasticity and aspect ratio of the channels. For example, an initially Newtonian-like flow could develop into a corner vortex directly or could develop first into a lip vortex, a divergent flow, and then into a corner vortex.

There are relatively few studies on the flow of particulate suspensions despite the fact that they are widely used in industry. The flow behaviors of the suspensions inside slit channels have been examined by a few researchers [16, 17]. Most particles have charges on their surfaces when dispersed in water. The electric potential at the slipping layer of a particle is known as the zeta potential [18]. In a suspension consisting only of particles and solvent, the particles are well dispersed when the absolute value of the zeta potential is large. In contrast, the particles can be coagulated when the value is small or zero. Complex flow behaviors, such as yielding and shear banding, can be observed depending on the dispersion state [16, 17]. However, a suspension consisting of particles as well as polymers shows more complicated behaviors. When a polymer moves close to a particle, the polymer can be adsorbed onto the surface of the particle by the van der Waal force,

hydrogen bonding, or electrostatic attraction. The extent of polymer adsorption onto particles depends on the interaction between the particles and the polymers [19-26]. Although it is important both in industry and academia to understand how the microstructure of a suspension consisting of both particles and polymers influences the rheological properties and the flow behaviors in a complex geometry, it has rarely been studied systematically.

Clogging mechanism

A membrane carries numerous pores and the flow through this pore can be represented by a flow through a single contraction channel [27, 28]. When a fluid flows inside a single micro pore, various flow behaviors, such as elastic vortex, divergent flow and extra pressure drop, can be observed depending on the properties of the fluid, flow rate, and the shape of the channel as mentioned above [2, 4, 11]. Also, Han et al. studied the flow of alumina suspension in the contraction channel [17]. The effect of polymer-particle interaction on the fluid dynamics in micro contraction geometry was also studied [29]. The common feature in these studies is that the particles did not adsorb onto the wall.

However, it is typical that the particles deposit on the wall of a channel, and the retention of particles cause several problems, such as pressure drop, clogging or fouling. To prevent a fouling problem, patterned membranes [30-32] or self-cleaning membranes [33] have been applied. It is important to understand how a membrane is fouled or clogged and

how they block the channel, which is very complicated. There have been many studies on clogging [27, 28, 34-41]. Ramachandran and Fogler [41] studied that the clogging formation of particles smaller than the pore size originates from the hydrodynamic bridging in dead end filtration. Although the particle size is smaller than the pore size, the clogging was built up by the hydrodynamic bridging and the pressure drop increased when the hydrodynamic force was strong enough to overcome the interparticle and particle-pore surface colloidal repulsion. In clogging or fouling, colloidal interactions play an important role. When the particle mass flux cannot overcome the particle-pore surface force, the particles cannot deposit on the wall. This concept is referred to as the critical flux density [42]. Agbangla et al. [34] studied the effect of the volume fraction of the particles, flow rate, and the properties of the particle on the clogging process both in the dead-end mode and in the cross flow mode. When the flow was slow or the volume fraction of the particle was low, the clogging did not take place. Brans et al. [43] studied the effect of transmembrane pressure (TMP) on the transmission of a micro-sized particle suspension. At low TMP, minimal adsorption and blocking was observed, and stable flux and full transmission was maintained. As TMP increased, the value of transmission changed and it finally decreased to zero for high TMP due to the formation of bridging.

The particle-wall interaction had an influence on the clogging process [44, 45]. For a PDMS channel treated with KCl, the channel became hydrophobic and the particles formed dendrites. On the other hand, for a PDMS channel treated with water, the channel was hydrophilic and a

bridging between the patterns was built up by the particles. The shape of a membrane affected the process how the particles stacked up. For a straight channel, dendrites were formed on the top of the wall while the particles clogged inner and outer channels for connected and staggered channels [35]. The extent of clogging was also different due to their different shape. The effect of entrance angle on the clogging rate was also analyzed based on transition-state theory [38]. When adding a surfactant to control the particle-particle interaction, this model predicted significant decrease in aggregation time and showed a good agreement with experimental data. The interplay between hydrodynamic conditions and colloidal interactions on the particle deposition in the pores was also investigated [46, 47]. Depending on flow conditions and ionic strength, the shape of the aggregates was changed. For a strong repulsive particle, a corner-shaped aggregate was formed while various shapes of aggregates were observed for large ionic strength. The erosion of the aggregates at high Péclet number and the steady shape of aggregates were observed [46]. It was also reported that high flow rate not only overcomes the particle-particle repulsive force but also breaks up particle-wall bonding, resulting in the delay of clogging [47]. When there exists a significant secondary energy minimum, a consequential clogging delay was observed. Therefore, it is important to understand the role of the hydrodynamic force and physiochemical interactions in order to figure out the clogging mechanism. To elucidate the clogging mechanism, the clogging process in a single pore needs to be studied [27, 28]. Dersoir et al. [27] reported that the length of clog was equal to the width of pore, and the aspect of

clog was changed with the pressure applied.

However, the factors, such as the volume fraction of particles or the particle-particle interaction, do not affect the clogging mechanism individually. For example, the clogging was easily formed as the volume fraction of the particle increased [34]. However, the viscosity can be increased too when the volume fraction increased further, which can have an influence on the particle deposition as well as on the hydrodynamic force. Also, the suspension can have the elasticity depending on the volume fraction and the type of the fluid. Although the viscosity and the elasticity of the fluid can have a strong influence not only on the fluid dynamics but on the clogging process, there exist few studies on the effect of the rheological properties of the fluid on the clogging.

Agglomerate breakup

The formation and breakup of a cluster of aggregates in a flow have drawn attention in both experiments and numerical simulations [48-60]. Aggregation is formed by reducing the electrostatic repulsion with suitable salts or depletion attraction with to a small amount of polymer, and it has a fractal-like structure [59, 61]. When it is exposed to a flow, it experiences deformation and breakup. The breakup in shear flow has been studied intensively [48, 62, 63]. However, the study on the breakup of agglomerates under the extensional flow has rarely been performed. The breakup of aggregation in mixed flows that can be

observed in contraction channel or nozzle has been explored recently [54, 57, 58, 60]. However, in contraction flow, the extensional flow is significant just right before and after the contraction throat, and shear flow is still dominant in upstream and downstream [57]. In addition, the capillary breakup extension rheometer (CaBER), which can be used to generate a uniaxial flow experimentally, has a disadvantage in that the flow cannot reach the steady state [64]. Thus, in the previous experiments using extensional flows, the time, during which an agglomerate can experience the extensional flow, is too short or it is not suitable to observe the behavior of the aggregation. As a way to overcome these problems, a cross channel which generates a planar extensional flow can be used [65].

In this thesis, the dynamics of particulate suspensions in complex flow, which includes vortex formation, channel clogging, and agglomerate breakup, was studied. Firstly, by comparing the rheological properties and vortex development of silica/PEO suspensions with those of PEO solutions, the effect of silica particles on the rheological properties and vortex dynamics was examined. Secondly, as a first step to examine how rheological properties of the fluid have an influence on the clogging mechanism, the effect of the fluid viscosity on the clogging of poly(styrene) particles inside a single pore was investigated. Lastly, the breakup of a single agglomerate under purely extensional flow was studied.

1.2 Outline of the thesis

The objective of this thesis is to study the dynamics of particulate suspensions in complex flow including vortex formation, channel clogging, and agglomerate breakup.

In section 2, the experimental set-up will be introduced. In this studies, two different type of channels were employed: first is the contraction channel and the other is the cross channel. So, in section 2.1, how to generally fabricate a micro channel is described and the specific geometry of channels is dealt with in each topic. In section 2.1, the observation system to observe the flows or the agglomerate behaviors is shown.

In section 3, the effect of silica particles on vortex dynamics of poly(ethylene) oxide solutions is examined. In this section, the vortex development in PEO solutions will be explored. The vortex development characteristics of silica/PEO suspensions will then be demonstrated to show the effect of silica particles, after which the rheological properties and the amount of adsorption are investigated in an effort to explain the vortex behaviors.

Section 4 describes the effect of the fluid viscosity on the clogging of poly(styrene) particles inside a single pore. In this section, notable behaviors during the clogging process and the relationship between the deposition of particles and pressure drop will be explored. Then, the effect of the shear force on the clogging pressure drop will be treated.

Section 5 quantitatively analyzes the breakup process of the aggregation under the extensional flow. In this section, the behavior of

a single agglomerate at stagnant point was observed. The fragment area showed a power-law relationship with the applied stress, which was in good agreement with a model prediction.

Chapter 2.

Experiment section

2. Experiment section

2.1 Channel fabrication

In this thesis, micro channels, such as contractions and a cross-shaped geometry were used to observe flows and agglomerate behaviors inside channels. In this section, the way to fabricate the channel is described and the specific geometries will be introduced in each topic.

The mold of the micro channel was made with typical photolithography method by using a SU-8 photo resist and a chrome mask [66, 67]. The micro contraction channel was fabricated by using poly(dimethyl siloxane) (PDMS, Sylgard 184A, Sewang Hitech Silicone, Korea). PDMS and curing agent (Sylgard 184B, Sewang Hitech Silicone, Korea) were pre-mixed with the ratio of 10 to 1, and the mixture was used after removing bubbles by a vacuum pump. PDMS was evenly coated on a cover-glass using a spin-coater and was poured onto an SU-8 mold. Both the PDMS coated cover-glass and mold were pre-baked in an oven at a temperature 80 °C for 20 min. After softly cross-linked PDMS which was separated from the mold was placed on the PDMS-coated cover-glass, the channel was left in the oven overnight. This PDMS-fabricated channel is known to be hydrophilic [68]. Because the

channel is transparent, it is suitable to observe the flow or clogging inside the channel.

2.2 Observation system

To observe inside the channels, the inverted microscopy, IX-71 (Olympus, Japan) was used. The light from a halogen lamp was illuminated above the channel and the flow inside channel was monitored by a lens with various magnification below the channel (Fig. 2.1).

In section 3, to monitor the streamlines of the flow, 0.03 wt% of 1 μm carboxylate-modified red fluorescent particles (excitation/emission = 520/580 nm) were introduced. The light from the mercury lamp used in this study (Olympus, Japan) had a wavelength of 530 nm, with the light filtered by an XF102-2 filter (Omega Optical, USA) with illumination onto the contraction part.

To record flows inside channels, CCD camera or high-speed camera were adopted. CCD camera (resolution: 1000 x 1000 pixels) (Hamamatsu, Japan) was highly sensitive. For a high-speed camera (Photron Fastcam Ultima 512, Photron Inc., USA), the frame rate was 2000 fps, and the camera resolution was 512 x 512 pixels, covering 392.7 x 392.7 μm^2.

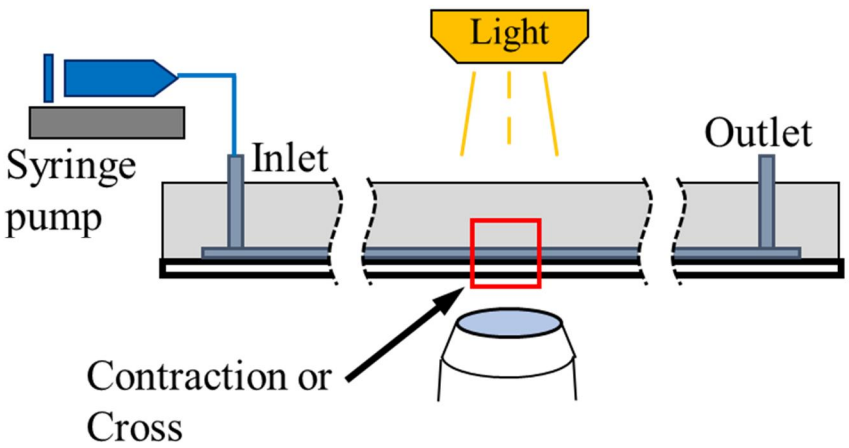

Fig. 2.1 Observation system. Contraction or cross geometries were used. Depending on channels, the number of inlets and outlets is different and it is dealt with in each section.

Chapter 3.

Effect of silica particles on vortex dynamics of poly(ethylene) oxide

solutions

3. Effect of silica particles on vortex dynamics of poly(ethylene) oxide solutions

3.1 Experimental

3.1.1 Materials

The silica particles used in this study were synthesized by the Stöber method [69]. First, 250 ml of anhydrous ethyl alcohol (Daejung, Korea) and 27 ml of an ammonia solution (28 wt%, Aldrich, USA) were mixed for 20 minutes. Then, an amount of 15.6 ml of tetraethoxysilane (Aldrich, USA) was quickly added and the mixture was stirred at room temperature for four hours. A magnetic stirrer was used, and the mixing rate was fixed at 500 rpm in all mixing steps. After the synthesis step, the particles were washed three times in absolute alcohol. Well-dispersed silica particles could then be obtained by washing the particles with water four times. The diameter of the silica particles was approximately 260 nm, as shown in the SEM image in Fig. 3.1. Silica particles are known to have a negative zeta potential in a wide range of pH levels [70]. Using zeta-potential & particle size analyzer ELS-Z (Otsuka Electronics, Japan), the zeta potential was measured and found

to be negative from pH 3 to pH 11 (Fig. 3.2). The BET surface area of the particles was 143.85 m^2/g.

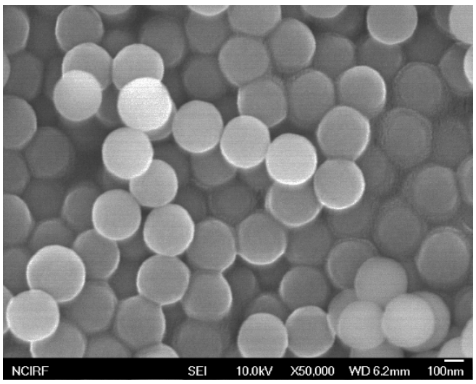

Fig. 3.1 SEM image of the synthesized silica particles (average diameter = 260 nm, standard deviation =11.7 nm).

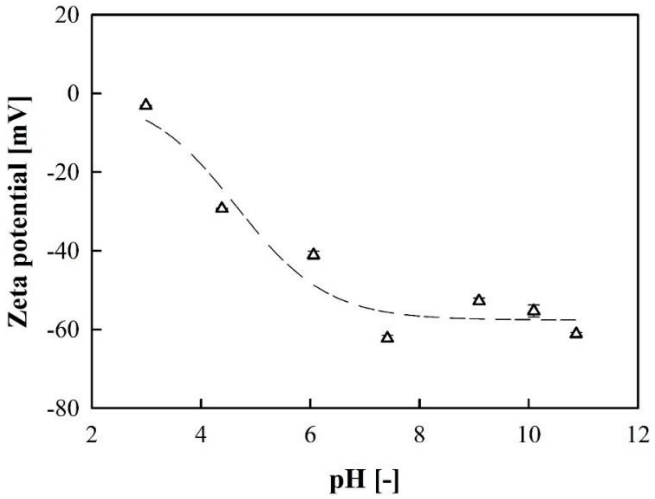

Fig. 3.2 Zeta potential of the synthesized silica particles (error bars included). The dotted line is a simple guide line.

Poly(ethylene oxide) (Sigma-Aldrich, USA, Mw=2,000,000 g/mol) was used as a polymer. PEO adsorbs onto the surface of silica due to hydrogen bonding. This mechanism was explained in previous studies [19-21]. To observe the vortex development of PEO solutions without silica particles, 0.6, 0.8, and 1.0 wt% of PEO solutions were used, with the samples labelled as PEO0.6, PEO0.8 and PEO1.0, respectively. To investigate the effect of silica, the PEO concentration was fixed at 1.0 wt% and silica concentrations of 1.0, 2.0, 4.0, and 8.0 wt% were used, with labels of PEO1.0_S1.0, PEO1.0_S2.0, PEO1.0_S4.0, and PEO1.0_S8.0, respectively. PEO0.6_S1.0 and PEO0.85_S1.0 denote the suspensions of 1 wt% silica in the 0.6 and 0.85 wt% PEO solutions, respectively (Table 3.1).

Table 3.1. Sample names, concentrations, rheological properties and the adsorption of polymer per unit area. η_0 is the zero-shear viscosity, G' is the storage modulus at a frequency of 10 rad/s, λ denotes the characteristic relaxation time (measured by CaBER) and Γ is the amount of adsorbed polymer per unit area (measured by zeta-potential & particle size analyzer ELS-Z).

Name	PEO conc. [wt%]	Silica conc. [wt%]	η_0 [Pa s]	G' [Pa]	λ [ms]	Γ [mg/m^2]
PEO0.6	0.6	0.0	0.040	0.076		-

PEO0.8	0.8	0.0	0.095	0.23		-
PEO1.0	1.0	0.0	0.20	0.48	40	-
PEO1.0_S1.0	1.0	1.0	0.15	0.36	24	3.0
PEO1.0_S2.0	1.0	2.0	0.22	0.44	32	1.5
PEO1.0_S4.0	1.0	4.0	0.33	0.70	43	0.8
PEO1.0_S8.0	1.0	8.0	0.61	1.20	77	0.4
PEO0.6_S1.0	0.6	1.0	0.033	0.049		1.7
PEO0.85_S1.0	0.85	1.0	0.11	0.078		2.6

To produce the silica/PEO suspensions, pre-calculated amounts of polymer were dissolved in distilled water overnight. In each case, the silica suspension was well dispersed in water and was used after being dispersed by sonication for 30 minutes. After a pre-calculated amount of the silica suspension was added to the PEO solution, mixing took place under a mild condition using a magnetic stirrer for 48 hours. It was confirmed that the adsorption process of PEO onto silica was completed within 24 hours. The amount of polymer adsorbed onto the silica particle per unit area was measured using a total organic carbon analyzer sievers 5310C (TOC, GE, USA), which can measure the carbon concentration in a sample. It was considered that the difference

between the initial concentration and the concentration of the supernatant solution as measured by the TOC system was equivalent to the amount of PEO adsorbed onto the silica particles.

3.1.2 Channel geometry

The micro-channel shown in Fig. 3.3 was designed and used. Here, W_u is the upstream width, W_d is the downstream width, and h is the channel height. W_u, W_d, and h are 400, 100, and 50 μm, respectively. The upstream length of the channel was 1 cm, which was enough to guarantee a fully developed flow. The downstream length was fixed at 3 cm, which was long enough to remove the influence of the vortex [12].

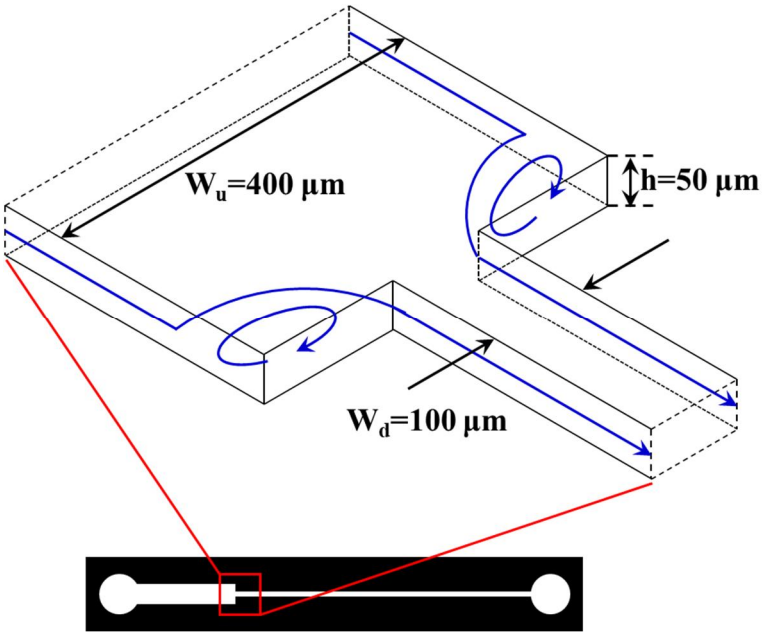

Fig. 3.3 Schematic of the 4:1 contraction channel: W_u = upstream width of the channel, W_d = downstream width, h = channel height.

3.1.3 Rheological measurements

A rotational rheometer DHR-3 (TA Instruments, USA) was employed to measure the viscosity and moduli of the polymer solutions and

silica/PEO suspensions. As both the viscosity and modulus are relatively low, a 60-mm parallel plate was used. All rheological properties were measured at 25 °C. To measure the material properties (the storage and loss modulus), a dynamic strain or stress sweep test was conducted at small strain amplitude (SAOS). It was not easy to get reliable data at low strain and low angular frequency, especially for low PEO concentration. The condition (the strain 10 % and the angular frequency 10 rad/s) was set to guarantee linear viscoelasticity with good data reliability.

The relaxation time of the sample was measured using a capillary break-up extensional rheometer (CaBER, Haake, USA). Reproducible and reliable relaxation time of semi-dilute and low viscous solutions could be measured [71]. The dimensionless numbers were calculated with these relaxation times (see section 3.1.4). The viscosity, storage modulus, and relaxation time of each sample are given in Table 3.1.

3.1.4 Dimensionless numbers

To characterize the dynamics of the flow passing through the micro-contraction channel, the Weissenberg number (*Wi*) and Reynolds number (*Re*) were introduced [9, 11]. First, the Reynolds number is the ratio of the momentum force to the viscous force. It is defined as follows,

$$Re = \frac{\rho \bar{V}_c D_h}{\eta_0} = \frac{2\rho Q}{(W_d + h)\eta_0},$$

where ρ is the fluid density, η_0 is the zero-shear viscosity, $\overline{V_c} = Q/(W_d h)$ is the average velocity, and $D_h = 2W_d h/(W_d + h)$ is the hydraulic diameter.

The Weissenberg number is defined as the product of the characteristic time of the material and the characteristic rate of deformation:

$$Wi = \lambda\dot{\gamma} = \frac{\lambda\overline{V_c}}{W_d/2}$$

Here, λ is the characteristic (relaxation) time and $\dot{\gamma}$ is the shear rate.

For the PEO1.0 solution, the zero-shear viscosity was 0.2 Pa·s and the relaxation time was approximately 40 ms. When the flow rate is 5ml/hr, the Reynolds number and Weissenberg number are 0.09 and 222.2, respectively. Because the Reynolds number is very small and the Weissenberg number is large, the elasticity dominates the fluid dynamics in this system.

3.2 Behavior of PEO solution

First, the vortex development in the poly(ethylene oxide) solutions without silica particles in the contraction channel was observed. The concentration of the PEO solution was varied from 0.6 to 1.0 wt%. For PEO with a molecular weight of 2 million, the calculated overlap concentration (c^*) was 860 ppm according to $c^* = 0.77/[\eta] = 0.77/0.072M_W^{0.65}$ [72, 73]. Here, M_W is the molecular weight and $[\eta]$ is the intrinsic viscosity. As a result, the

concentration was semi-dilute and was approximately ten times higher than the overlap concentration. For a low concentration of PEO solution (approximately 0.3 wt% and below), a vortex did not appear under the tested conditions. For higher concentrations, a considerable amount of time was needed to dissolve the polymer, and it was difficult to obtain a homogeneous sample.

Fig. 3.4 shows the vortex sizes of the 0.6, 0.8 and 1.0 wt% PEO solutions versus the flow rate. For the PEO1.0 solution (triangle symbol), the vortex gradually developed as the flow rate was increased. When the flow rate was low, the vortex did not appear, as shown in Fig. 3.4(a); this state is known as a Newtonian-like flow. Thus, the vortex size cannot be measured until a specific flow rate is reached. When the flow rate was larger than 0.3 ml/hr, a vortex appeared next to the throat of the contraction; this type of vortex is termed a lip vortex (Fig. 3.4(b)). The lip vortex expanded towards both the upstream and corner directions with an increase in the flow rate. When the lip vortex develops such that it is located at the corner, it is referred to as a corner vortex (Fig. 3.4(c)). After the formation of the corner vortex, the vortex grew toward the upstream direction. This vortex sequence is in good agreement with earlier findings [15].

The flow rate at which a lip vortex or corner vortex was formed was found to depend on the properties of the fluid, while the vortex developed in the same sequence for different concentrations. As shown in Fig. 3.4, the higher the PEO concentration was, the larger the vortex became due to the high degree of elasticity.

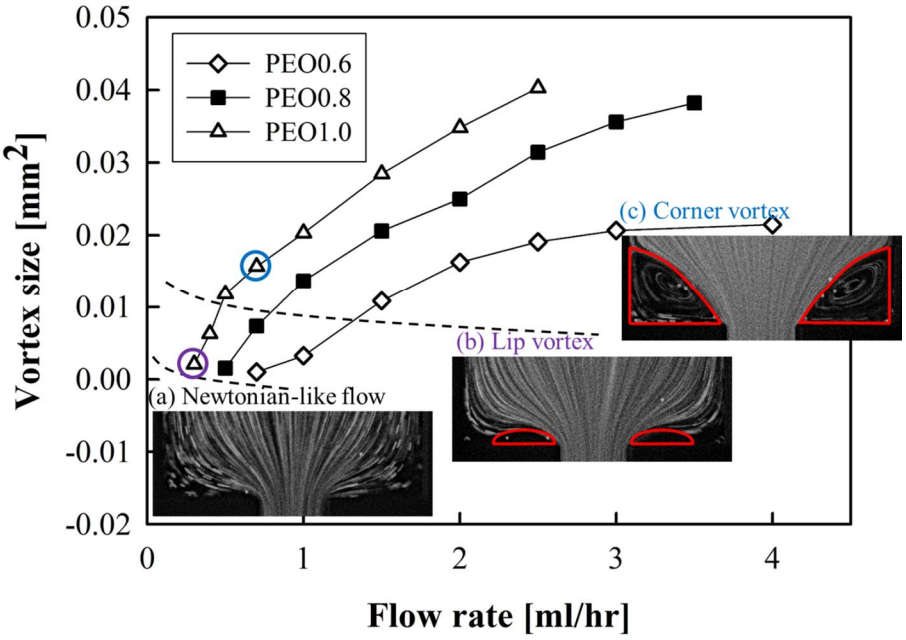

Fig. 3.4. Vortex development of PEO solutions as a function of the flow rate. The images are for PEO concentration of 1.0 wt%: (a) Newtonian-like flow at Q=0.2 ml/hr, (b) lip vortex at Q=0.3 ml/hr, and (c) corner vortex at Q=0.7 ml/hr.

3.3 Behavior of PEO/silica suspension

First, a sedimentation test was conducted on all samples to assess the

stability of the suspensions. A vial with a diameter of 19 mm and a volume of 12 ml was filled with the suspension and then left undisturbed. The silica alone without polymer completely settled down in three days, whereas the silica in all silica/PEO suspensions did not settle down, even after a month. Also, in each case, the particles observed in the cryo-SEM were well dispersed. In other words, the stability of all the samples was guaranteed.

3.3.1 Vortex development

Similar to PEO solutions, the vortex in the suspensions increased with an increase in the flow rate. The overall vortex shape of the suspensions looked similar to that of the PEO solution. In addition, it was Newtonian-like flow initially, in which the vortex did not form at low flow rate and then formed as a lip followed by a corner vortex. Thus, the addition of silica particles did not have any influence on the vortex sequence.

On the other hand, the particle affected the vortex size. It also changed the flow rate at which the lip vortex formed and developed into a corner vortex. To understand the effect of silica particles, the vortex development was observed as the silica concentration was increased from 0.0 to 8.0 wt% while fixing the PEO concentration at 1.0 wt%. Fig. 3.5(a) shows the vortex size as a function of the Weissenberg number which was calculated using the CaBER relaxation time. As shown in Fig. 3.5(a), the lip vortex grew with increasing the

Weissenberg number approximately from 10 to 20, while the corner vortex developed at the Weissenberg number larger than 20. It is interesting to note that in most cases, the slope of the vortex size changed at the point where the lip vortex developed to the corner vortex. For an easier comparison of the vortex size, all vortex sizes were normalized with the vortex size of the PEO1.0 solution at an identical flow rate (Fig. 3.5(b)). For the suspensions with silica concentrations of 1.0 and 2.0 wt%, the vortex was smaller than that of the PEO1.0 solution. When the concentration of silica increased further, the vortex size increased and became larger than that of the PEO solution (Fig. 3.5(b), 4.0 and 8.0 wt%). When the flow rates were 1.0, 1.5, and 2.0 ml/hr, the curves for the normalized vortex size overlapped regardless of the flow rate. In contrast, the normalized vortex size with silica concentrations of 1.0 and 2.0 wt% did not overlap with each other, as a lip vortex formed for PEO1.0_S1.0 and PEO1.0_S2.0, whereas the vortex had already developed as a corner vortex for PEO1.0_S4.0 and PEO1.0_S8.0 when the flow rate was 0.5 ml/hr.

As the concentration of silica influences the vortex size, it also affects the flow rate at which the lip vortex is formed and the flow rate at which the lip vortex develops into a corner vortex. For the PEO1.0 solution, the lip vortex had already appeared at a flow rate of 0.3 ml/hr. However, the lip vortex was observed at 0.5 ml/hr for the suspension containing 1.0 wt% of PEO and 1.0 wt% of silica (PEO1.0_S1.0). When the silica concentration increased to 2.0, 4.0, and 8.0 wt%, the flow rates at which the lip vortex formed were found to decrease to 0.4, 0.3, and 0.2 ml/hr, respectively. Similar to the lip vortex, the flow rate

at which the lip vortex developed into a corner vortex also changed according to the silica concentration. While the flow of PEO1.0 had already led to the formation of a corner vortex at a flow rate of 0.5 ml/hr, the flow of PEO1.0_S1.0 developed into a corner vortex at 0.7 ml/hr. With an increase in the silica concentration, the flow rate at which the corner vortex formed decreased again (0.7 ml/hr for PEO1.0_S2.0, 0.5 ml/hr for PEO1.0_S4.0 and 0.4 ml/hr for PEO1.0_S8.0).

In other words, the silica concentration has an influence on both the vortex size and the flow rate at which the lip or corner vortex was formed when the PEO concentration was fixed at 1.0 wt%. Depending on the silica concentration, the vortex size decreased and then increased while the flow rate at which a lip or corner vortex was formed increased and then decreased.

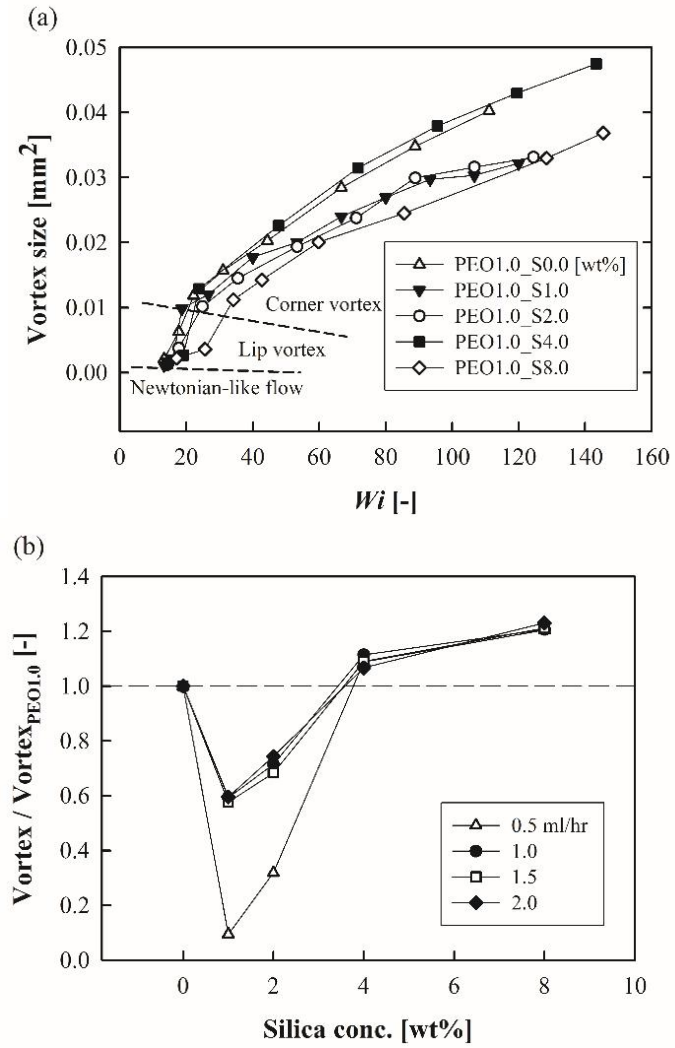

Fig. 3.5 (a) Vortex size of PEO/silica suspensions as a function of Weissenberg number. (b) Normalized vortex size of the suspension relative to the vortex size of the PEO solution. The PEO concentration was 1.0 wt% and silica concentration varied from 0 to 8.0 wt%.

3.3.2 Effect of viscoelasticity

Fig. 3.6(a) shows the shear viscosity of the suspensions. Strong shear-thinning is observed for all the samples. For the suspension with a silica concentration of 1.0 wt%, the viscosity was lower than that of the polymer solution without silica [21], while the viscosity of the PEO1.0_S2.0 suspension was comparable to that of the PEO1.0 solution. On the other hand, a gradual increase in the viscosity was observed for the suspensions containing 4.0 and 8.0 wt% of silica. Although the viscosity of PEO1.0_S1.0 was lower than that of PEO1.0 and the viscosity of PEO1.0_S2.0 was similar to that of PEO1.0 (Fig. 3.6(a)), the growth in the size of the vortex for these two suspensions (PEO1.0_S1.0 and PEO1.0_S2.0) was less than that of the PEO1.0 solution (Fig. 3.5(b))

In addition to the viscosity, the elasticity affects the vortex development. The storage modulus was measured to estimate the elasticity. As shown in Fig. 3.6(b), the storage moduli of the two suspensions composed of 1.0 and 2.0wt % silica particles were smaller than that of the pure PEO solution. In contrast, the storage moduli of PEO1.0_S4.0 and PEO1.0_S8.0 were larger than that of the PEO1.0 solution. This tendency is consistent with the vortex size.

The relaxation time also showed a trend similar to that of the storage modulus. As shown in Table 3.1, the relaxation time of PEO1.0 was approximately 40ms. The relaxation times for the suspensions with 1.0 and 2.0 wt% silica were 27 and 32 ms, respectively. However, when the silica concentration was 4.0 and 8.0 wt%, the relaxation time was larger

than that in the PEO1.0 case (Table 3.1); this tendency is in excellent agreement with the storage modulus data (Fig. 3.6(b)).

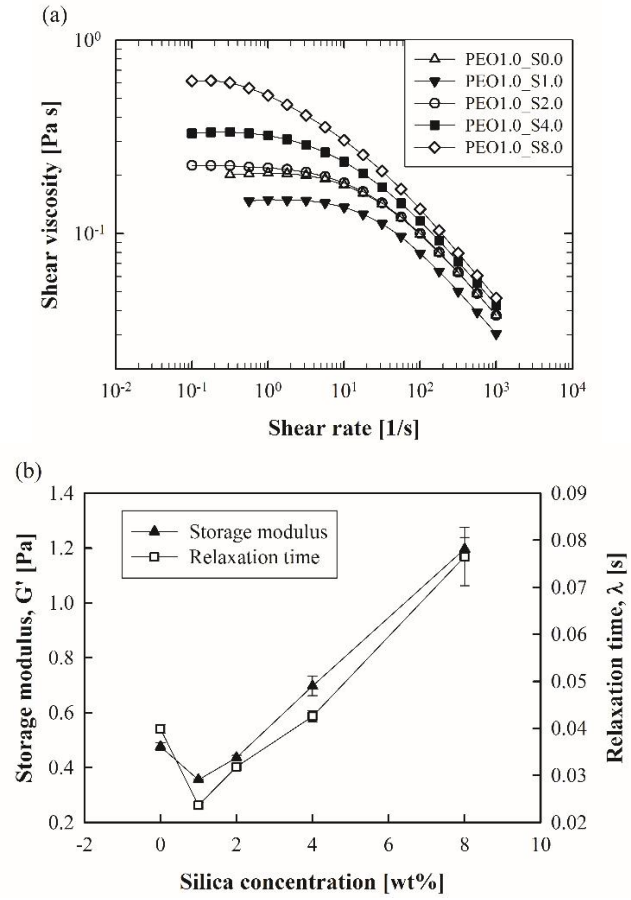

Fig. 3.6. Rheological properties of PEO/silica suspensions: (a) shear viscosity as a function of shear rate, (b) storage modulus (G') and relaxation time (λ) as a function of silica concentration. The PEO concentration was 1.0 wt% and the silica concentration was varied from 0.0 to 8.0 wt%. Error bars are included in (b).

It was reported that the viscosity decreases and then increases with an increase in the PEO concentration when the silica concentration is fixed; the decrease in the viscosity with an initial increase of the PEO dosage is attributed to steric hindrance arising from the polymers being adsorbed onto the surface of the particles [17]. Likewise, the adsorption of PEO onto the surface of silica particles can affect not only the viscosity but also the storage modulus.

3.4 Adsorption of polymer

The amount of adsorption per unit area of each sample is shown in Table 1. The amount of adsorption was 3.0 mg/m^2 when the PEO concentration and the silica concentration were both 1.0 wt%. In previous studies, though the amount of adsorption depended on the molecular weight of PEO and the size of the silica particles, the value was approximately 1.0 mg/m^2 [19, 20]. It was also reported that the amount of adsorption reached 2.5 mg/m^2 [74]. Though the amount of adsorption in this study is larger than those in previous results, it does not deviate significantly.

As shown in Table 3.1, the amount of adsorption decreased with the increase in silica concentration because the amount of adsorption per unit area depends on the ratio of the polymer to the silica particles. When the particle concentration is constant, the amount of adsorption usually increases with the polymer-to-particle ratio. When this ratio exceeds a specific value, no additional sites for polymer adsorption remain, with adsorption thus reaching the saturation point. The amount of adsorption can be calculated by dividing the total amount of

adsorbed polymers by the total area of the particles. Because the density of silica is roughly 2 g/cm^3, 1.0 wt% of silica is equivalent to 0.5 vol%. When 0.5 vol% of silica particles is dissolved into water, there is no distinguishable difference in the viscosity from that of water. (At 25 °C, the viscosity levels of water and of the suspension consisting of 0.5 vol% of silica were 8.52 mPa·s and 8.55 mPa·s, respectively.). On the other hand, the viscosity and storage modulus of the suspension with 1.0 wt% of PEO and silica decreased by as much as 27 and 25%, respectively. It can be considered that this change arises from the interaction between the polymer and the particles; that is, PEO adsorbs onto the surface of the silica particles.

When 1.0 wt% of silica was added, some of the polymer in the medium was adsorbed onto the silica and the amount of free polymer decreased. Because the amount of adsorption per unit area was 3.0 mg/m^2 with 1.0 wt% of silica (Table 3.1) and given that the surface area of the silica particles was approximately 143.85 m^2/g, the total amount of adsorption was approximately 0.43 g/100 g suspension, indicating that the mass of silica was 1 g and the amount of adsorption was 0.43 g when the total mass of the suspension was 100 g. This corresponds to 43% of the initial polymer concentration. Therefore, the polymer concentration in the medium was only 0.57 wt%. The storage modulus for 1.0 wt% of PEO solution was 0.48 Pa, while that of PEO0.6 (~0.57 wt%) was 0.076 Pa, which is only 16% of the value for PEO1.0. The decrease in the storage modulus arises from the decrease in the polymer concentration in the medium, however, the adsorbed polymer remains on the surface of the particles. Thus, the storage modulus did not

decrease to the degree noted with PEO0.6, but it did reach 75% of the value for PEO1.0, i.e., about 0.36 Pa.

When the silica concentration was 2.0 wt%, the total amount of adsorption was 0.43 g/100 g suspension (Table 3.1). Likewise, the total amount of adsorption was 0.46 g/100 g suspension with both 4.0 and 8.0 wt% of silica, and the total amount of adsorption remained nearly constant, at 0.43~0.46 g, regardless of the silica concentration. This result arose because the sites on which the polymers could adsorb increase with an increase in the number of silica particles despite the fact that the amount of adsorption per unit area decreases. Thus, the storage modulus increased because the number of silica particles with adsorbed polymers increased while the amount of free polymer in the medium remained nearly constant.

Extra polymer was added to compensate for the reduced free polymers due to adsorption and to confirm that the total storage modulus decreased due to the decrease in the amount of free polymer in the medium. For this purpose, the PEO0.6 solution and the PEO0.6_S1.0, and PEO0.85_S1.0 suspensions were compared. When 1.0 wt% of silica was added to 0.6 wt% of PEO solution, the amount of adsorbed PEO was measured and found to be 0.25 g/100g suspension. The proper amount of polymer corresponding to that amount was added, and the sample was denoted as the PEO0.85_S1.0 suspension.

Similar to the previous result, both the viscosity and the storage modulus decreased when an amount of 1.0 wt% of silica particles were added to 0.6 wt% of PEO solution (Fig. 3.7). For PEO0.85_S1.0, which

was compensated with additional polymer, the storage modulus recovered such that it was comparable to PEO0.6, although the viscosity increased by 2.8 times that of PEO0.6. The storage moduli of PEO0.85_S1.0 and PEO0.6 were 0.079 Pa and 0.076 Pa, respectively (Fig. 3.7(b)).

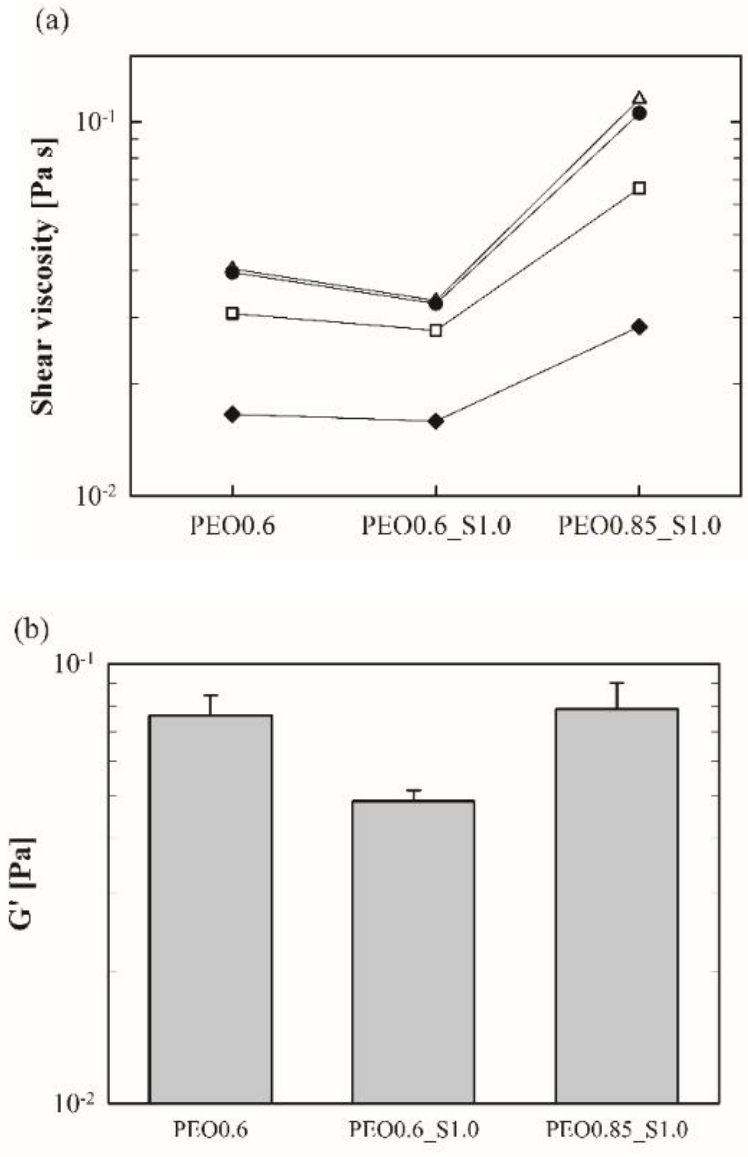

Fig. 3.7. Rheological properties of PEO/silica suspensions: (a) shear viscosity (Δ: 1.0, ●: 10, □: 100, and ◆: 1000 1/s) and (b) storage

modulus.

In addition, the vortex of PEO0.6_S1.0 was smaller than that of PEO0.6 (Fig. 3.8). Similar to the previous result, this arose because the polymers in the medium were adsorbed onto the silica and the amount of free polymers decreased. In contrast, the vortex of PEO0.85_S1.0, for which the effect of the lost free polymer was mitigated via additional polymer, developed in a manner similar to that of PEO0.6, as the polymer concentration in the medium in this case increased by compensating for the amount of adsorbed polymers.

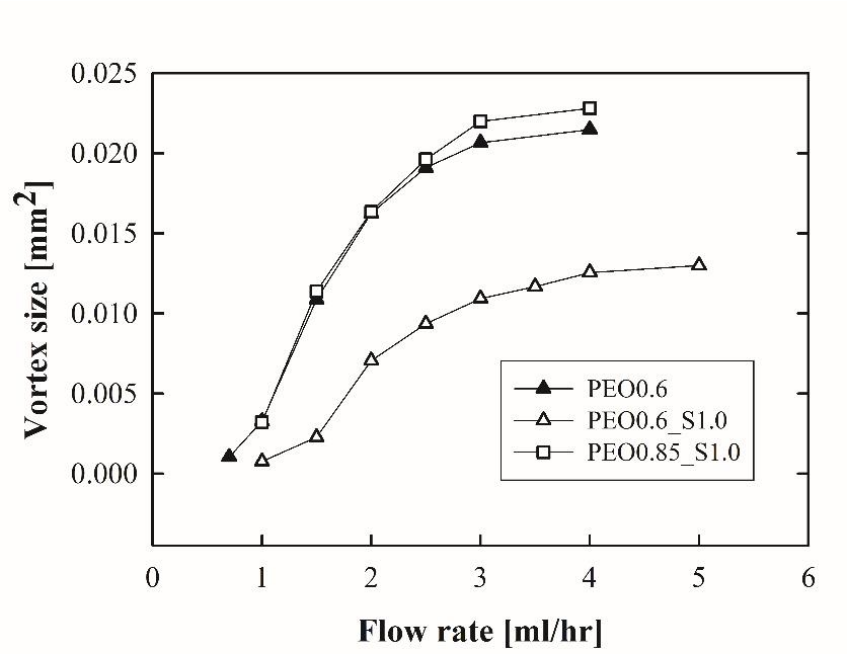

Fig. 3.8. Vortex size of PEO0.6, PEO0.6_S1.0, and PEO0.85_S1.0 as a function of flow rate.

Here, the correlation of rheological properties with the vortex development becomes more apparent. Although the viscosity levels of PEO0.6 and PEO0.85_S1.0 were different, it was observed that the vortices of the two samples developed similarly, from which it can be said that the fluid elasticity had a stronger influence on the vortex dynamics in the micro-contraction channel than the viscosity.

When 1.0 wt% of silica was added to the PEO solution, the modulus of the suspension decreased because the PEO in the medium was adsorbed onto the silica surface. At this point, the polymer concentration in the medium was only 0.57 wt%, which resulted in a decrease in the storage modulus. When the silica concentration increased to 2.0 wt% and surpassed that level, the total amount of adsorption rarely changed because the amount of adsorption per unit area decreased with an increase in the silica concentration. The storage modulus increased because more silica particles were added, while the amount of free polymer remained nearly constant.

The change in the storage modulus due to polymer adsorption influenced both the vortex size and the flow rate at which the lip vortex or corner vortex was formed. Although the amount of free polymer decreased when the particles were added to the PEO solution, the total storage modulus could be recovered with additional polymers corresponding to the amount of adsorbed polymer. Moreover, the vortex developed similarly with the recovery of the storage modulus.

From these results, it can be concluded that the addition of particles into a viscoelastic fluid does not monotonously increase the viscosity or the storage modulus of the suspension. It is important to understand the interaction between the polymer and the particles. When the polymer adsorbs onto a particle, the concentration of free polymer can vary, having a strong effect on both the rheological properties and the vortex development.

Chapter 4.

Clogging mechanism in contraction channel flow

4. Clogging mechanism in contraction channel flow

4.1 Experimental

4.1.1 Materials

A suspension was prepared by adding poly(styrene) particles into a glycerol solution, which is a Newtonian fluid. To control the viscosity of the Newtonian medium, the concentration of glycerol in DI water was controlled. The viscosity of glycerol solution was measured with DHR-3 (TA instruments, USA), which is a stress-controlled rheometer. A 60-mm parallel plate and peltier were used and the temperature was kept at 25 ℃. The viscosity behaved as a Newtonian fluid in which the viscosity does not change with the shear rate. The viscosity gradually increased with the increase in concentration of glycerol. The concentration of glycerol used in this study was 60, 70, and 80 wt. % and the shear viscosity was 8.7, 18.0, and 42.9 cp, respectively. The particle used in this study was poly(styrene) (PS) synthesized by the emulsifier-free emulsion polymerization [75]. The size of the particle was about 565 nm with high monodispesity, in which the standard deviation was about 9.6 nm. The PS particle was dispersed in DI water by sonication for 30 minutes before use. To make a suspension, a glycerol solution was prepared at a specific concentration. After pre-calculated amount of PS particles dispersed in water was added into the glycerol solution, the sample was mildly mixed (rpm=200~300) for one day. The pH of this PS-glycerol suspension was 4.5~4.7 and the zeta-

potential of PS particle in glycerol solution was -43.3 mV. The concentration of the particle was 0.05 wt. %. A vacuum adapter filter funnel (SciLab, Korea) with porosity of 16~40 μm was used to make sure that there was no aggregation, which can block the channel. For a convenience, glycerol solutions with the concentration of 60, 70, and80 wt. % were labelled as Gly60, Gly70, and Gly80, respectively. PS-glycerol suspensions were denoted by Gly60PS, Gly70PS, and Gly80PS according to the concentration of glycerol, respectively.

4.1.2 Channel geometry

A micro-contraction channel was employed to examine the clogging process of particles in a single pore (Fig. 4.1). W_u and W_d are the upstream and downstream width and they were 180 and 45 μm, respectively, which means that the contraction ratio was four. The channel height was 100 μm. The length of the upstream from inlet to contraction was 10 mm, and the length of the downstream from contraction to outlet was 15 mm (Fig. 4.1 (b)).

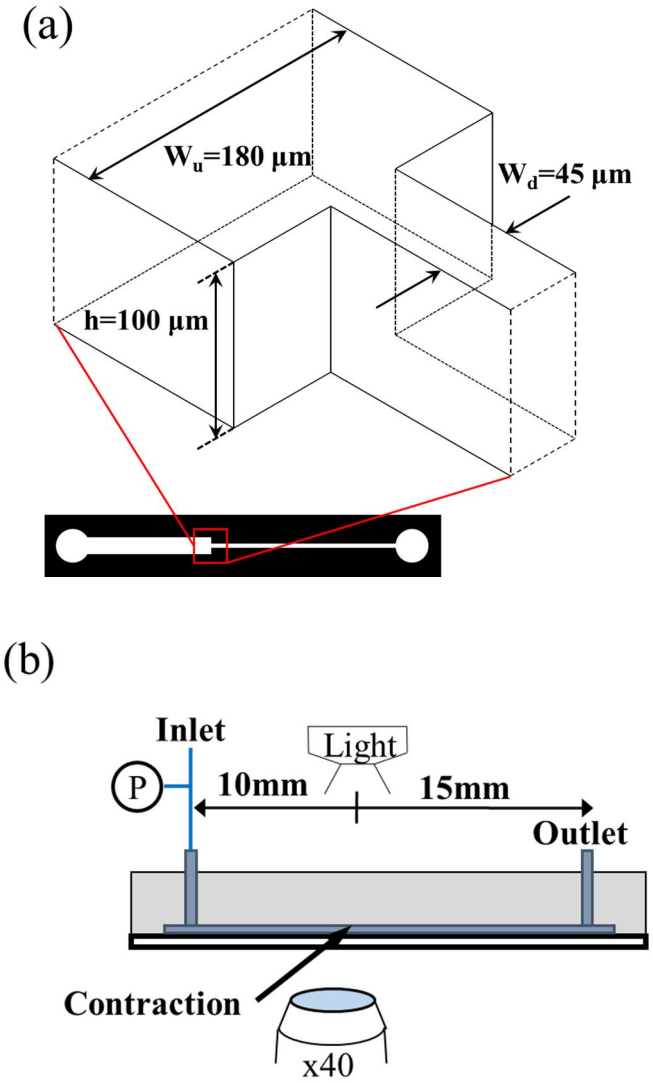

Fig. 4.1 (a) A detailed view of the 4 to 1 contraction channel; W_u = upstream width of the channel, W_d = downstream width, h = channel height. (b) Schematic of a channel and visualization system. Upstream

and downstream length were 10, 15 mm, respectively. ⓟ represents a pressure sensor.

4.1.3 Differential pressure drop measurement

In addition to capturing images by CCD camera, differential pressure drop was also measured to quantify the clogging process. For this, an uPS pressure sensor (LabSmith, USA) was used. Two types of sensors were employed according to the pressure range. One (uPS0250) could measure 0~250 kPa and the other (uP0800) has a range of 0~800 kPa. Although both sensors were used depending on the fluid and flow rate, uP0800 sensor was mainly used. The resolution of uP0250 and uP0800 was 1 and 5 Pa, respectively. The sensor was installed between a syringe and the channel inlet (Fig. 4.1(b)). Tygon tube was used to link between the syringe and the sensor, and between the sensor and the inlet. The outlet of the channel was left open. From this set-up, the clogging process could be monitored by measuring the differential pressure drop simultaneously with visual information taken by CCD camera. First, the pressure drop without PS particle was measured (Fig. 4.2(a)). To observe the clogging process and measure the pressure drop, the fluid was injected for a long time by a syringe pump (PHD4400, Harvard apparatus, USA). The pressure drop increased linearly with flow rate (Fig. 4.2(a)) [2, 11, 76]. The pressure drop can also be expressed as the product of flow rate and hydraulic resistance ($\Delta P = RQ$, where ΔP is the pressure drop, R is the hydraulic resistance, and Q is the flow rate.). Fig. 4.2(b) shows the medium resistance of solvent (glycerol solutions) (R_0) with flow rates. It was nearly constant

until a certain flow rate and then decreased. It is because the slope of the pressure drop decreased due to the swelling of the channel at high flow rates (Fig. 4.2(a)). Thus, in this study, the flow rate was limited to 1.5, 1.0, and 0.5 ml/hr for Gly60, 70, and 80, respectively.

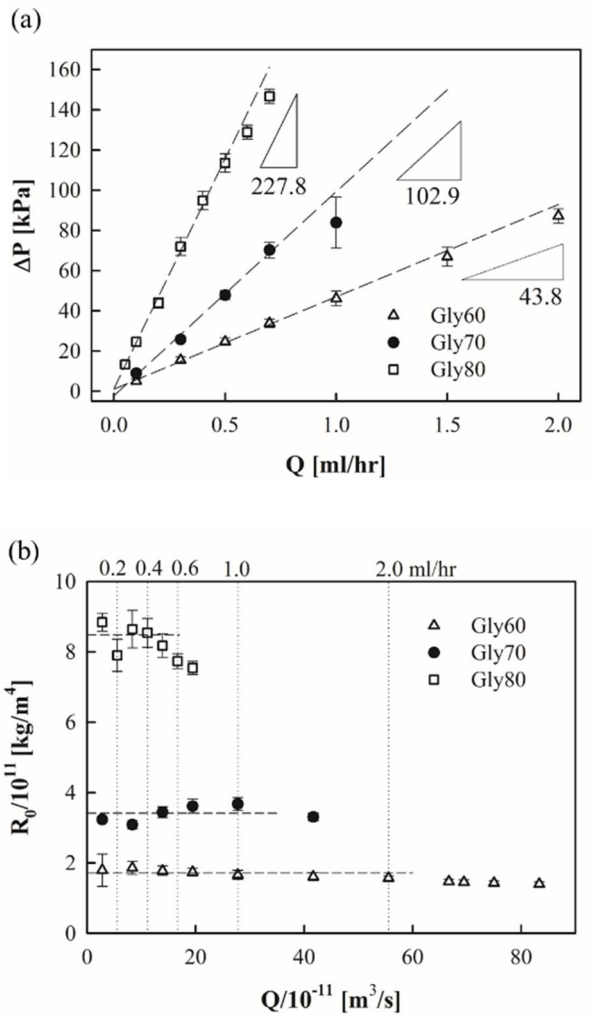

Fig. 4.2 (a) Differential pressure drop of glycerol solutions without PS particles. (b) The hydraulic resistance of glycerol suspensions with flow rate. The unit of flow rate is m^3/s. For convenience, the flow rate in ml/hr unit is also given on the upper x-axis (vertical dotted lines).

4.1.4 Operation conditions

The admissible range of the flow rate depends on fluid. In the case of Gly60PS, the experiments were possible over a relatively broad range of flow rates, from 0.3 to 1.5 ml/hr. The Reynolds number ($Re = \frac{\rho \overline{V_d} D_h}{\eta} = \frac{2\rho Q}{(W_d+h)\eta}$, the ratio of inertial force to viscous force, where ρ is the fluid density, η is the shear viscosity, $\overline{V_d} = Q/W_d h$ is the average velocity, and D_h is the hydraulic diameter.) corresponds to 0.20 to 1.0. For Gly70PS, the range was from 0.3 to 1.0 ml/hr ($0.10 \leq Re \leq 0.32$), and for Gly80PS, it was from 0.3 to 0.5 ($0.04 \leq Re \leq 0.07$). All experiments were conducted below Re ~ 1. Stokes number ($\mathrm{St} = \frac{\rho_p d_p^2}{18\eta} \frac{\overline{V_d}}{W_d}$, where ρ_p is the particle density, and d_p is the particle size) was also calculated in the order of $O(10^{-19}\text{-}10^{-18})$. Table 4.1 shows the viscosity and shear stress covered in this study with the flow rate of glycerol solutions without PS particles.

As mentioned before, the fluid was injected at a constant flow rate by using a syringe pump. While the rate of clogging varied according to the fluid and flow rate, the particles began to deposit on the channel wall right after the startup of a test in all cases. This was confirmed by both CCD camera and the pressure drop.

Table 4.1 The viscosity and shear stress at each flow rate of glycerol solutions. The shear stress is the product of the shear rate (in the parenthesis) and shear viscosity in Pa unit. Flow conditions that did not cause clogging are marked with grey boxes.

Fluid	η [cp]	σ [Pa]				
		Q=0.3 [ml/hr] ($\dot{\gamma}$=823.0 [1/s])	0.5 (1371.7)	0.7 (1920.4)	1.0 (2743.4)	1.5 (4115.2)
Gly60	8.7	7.2	11.9	16.7	23.9	35.8
Gly70	18.0	14.8	24.7	34.6	49.4	
Gly80	42.9	35.3	58.8			[Pa]

4.2 Clogging mechanism and pressure drop

Although the rate of clogging was different with different viscosity and flow rate, the overall behavior was similar. Fig. 3 shows the normalized pressure drop and the images over time when Gly70PS flowed at the flow rate of 0.3 ml/hr. The normalized pressure drop is the pressure drop of PS/glycerol suspension divided by the pressure drop at the same flow rate of the glycerol solution with no particle. The normalized pressure drop indicates how much the pressure drop was increased over the one without the particles. When Gly70 flowed with no particle at the same flow rate (0.3ml/hr), the pressure drop was maintained at 25.7 kPa (Fig. 4.2(a)) and the hydraulic resistance was $3.09 \cdot 10^{11}$ kg/m^4 (Fig. 4.2(b)). However, as shown in Fig. 4.3(a), the normalized pressure drop of Gly70PS showed a complex behavior while fluctuating up and down repeatedly over time. That is, the particle deposition has an influence on the pressure drop. Right after the test began, the pressure drop steeply increased. While the pressure drop of Gly70 (without particle) was about 25.7 kPa, the pressure drop of Gly70PS reached 25 kPa in 6.4 s and continuously increased. Here, the hydraulic resistance can be considered as the summation of the additional resistance, R_a and the medium resistance, R_0 ($\Delta P = (R_a + R_0)Q$). Because the pressure drop of glycerol solution is defined as $\Delta P_{Gly} = R_0 Q$, the relationship between the normalized pressure drop and the resistance ratio is given as $R_a/R_0 = \Delta P/\Delta P_{Gly} - 1$.

In Fig. 4.3(b), the dark area near the channel wall results from the PS

particles which were stuck to the wall. The particles started to deposit on the wall, especially in the downstream right after the contraction in early stage of the test. Here, it should be noted that the particles did not deposit at upstream in the beginning, but it deposited at downstream first. As time passed, the amount of particles deposited on the wall increased. In Fig. 4.3(b), the particles already deposited on the downstream wall after 2 min. As the wall was already coated with a layer of particles along the downstream, newly approaching particles stuck temporarily and detached by the flow, and rolled over the coated particles and flowed away, which is defined as “rolling” in this study. The extent of “rolling” is important because it can determine whether the channel will eventually be blocked or not. It was repeating that some particles were separated and flowed away from the wall while some particles were adsorbed on the wall and did not move. At 74 min, the accumulated area expanded over the entire contraction. Although some particles began to deposit at upstream, it did not block the entire channel, but simply sticking to the top or bottom of the channel (the size of particle was 565 nm and the channel height was 100 μm).

Although the accumulating particles appeared to block the contraction completely at 112 min, there was no complete clogging occurred. This is due to the fact that the images from the microscope are two dimensional. Still, the channel did not burst, and the pressure drop did not grow particularly large, as shown in Figure 4.3(a). Though it seems to be completely clogged in the images, in reality there was enough hole in the middle, allowing fluids to flow. It would be interesting to look at the clogged structure, but it was not possible to look inside the

structure with the inverted microscope. Therefore, measuring the pressure drop in addition to taking the images can be a complementary tool to examine the clogging mechanism.

The particles were then piled up in the upper part of the contraction, and the normalized pressure drop was maintained at around 2±0.5. Occasionally, as the amount of accumulated particles increased, the pressure drop suddenly increased, after which it dropped when the particles were removed from the contraction by the flow. As shown in Fig. 4.3(a), the peak appeared near 600 min. When the particles blocked the contraction as in image (5), the normalized pressure drop rapidly increased to about 5.2. This was about 5 times the pressure drop of 25.7 kPa where there was no particle.

For simplicity of calculation, assuming a straight square duct flow, we have a relation of $\Delta P \sim Q/A^2$ by the Hagen-Poiseuille equation. That is, the pressure drop is inversely proportional to the square of the cross-sectional area of the channel. A 5-fold increase in pressure drop means that the cross-sectional area of the channel has decreased by a factor of $\sqrt{5}$. Thus, when the particles were piled up and the effective area was reduced, a considerable increase in pressure drop could be observed. Since the syringe pump was used in this experiment, the fluid was pumped at a constant flow rate regardless of the pressure. In the image (6) after 622 min, the accumulated particles could not withstand the increasing pressure, and the large portion of the accumulated particles dropped off as an agglomerate and the pressure drop decreased sharply (Fig. 4.3 (a)). The implication here is that even if the particles in the

fluid were initially well dispersed, they may form a large agglomerate after the clogged particles were detached from the wall. The same behavior was repeated after the sudden increase in pressure drop followed by a decrease. As the particles accumulated again, the pressure drop increased significantly, and when the particles detached, it suddenly decreased showing a peak.

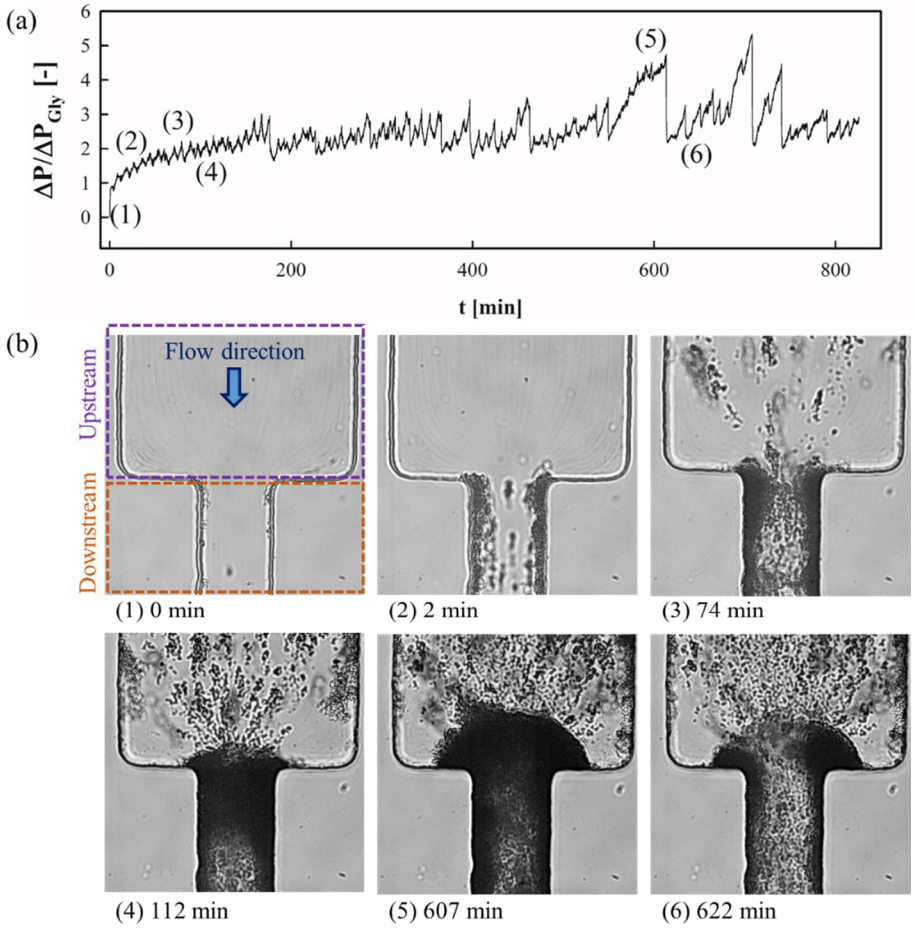

Fig. 4.3 (a) The normalized pressure drop of Gly70PS with time. The flow rate was 0.3 ml/hr. (b) Snapshots of the contraction part. (1) to (6) in figure (a) roughly show the time of snapshots in figure (b).

However, different behavior was observed above a certain flow rate. Fig. 4.4 shows the behavior of Gly70PS flowing at a flow rate of 1.0 ml/hr. For Gly70 with no particles at 1.0 ml/hr, the pressure drop was 83.9 kPa. In the presence of particles, the particles began to stick at the downstream in the beginning of the experiment. Similar to the previous results at 0.3 ml/hr, the particles first adhered at the downstream, after which the coming particles showed a "rolling" behavior. However, at a flow rate of 1.0 ml/hr, as shown in Fig. 4.4(b), only a small fraction of the contraction was accumulated even after 223 minutes due to the rolling behavior. If the "rolling" behavior occurs intensively, the channel clogging can be prevented or delayed.

In Fig. 4.4(b), image (1) and (2) were taken after 107 min and the red boxes on (1) and (2) are the enlarged images around the contraction. The particles were piled up at the left hand side of the upstream (1). The interval between the images (1) and (2) is about 1/30 s. After 1/30 s (image (2)), a "stick and detach" behavior, in which a part of the accumulated particles is removed by the flow, was observed. A small portion of the accumulated particles was removed continuously by "rolling" and "stick and detach", and the channel was not completely blocked after a long period of time (3). This behavior was also confirmed by pressure drop. As shown in Fig. 4 (a), after the startup of the experiment, the normalized pressure drop reached about 1 in 2.2 s. Thereafter, unlike the previous case, the ratio did not increase significantly but was maintained at 1. There was still particle deposition on the wall even though it was a small amount, and this might be the cause of the slightly higher pressure than that without particles. In

addition, there was no specific peak that was seen when the particles blocked the channel. The experiment was carried out for a relatively short time compared to 0.3 ml/hr due to the high flow rate, but the channel was not blocked even after 4 hours.

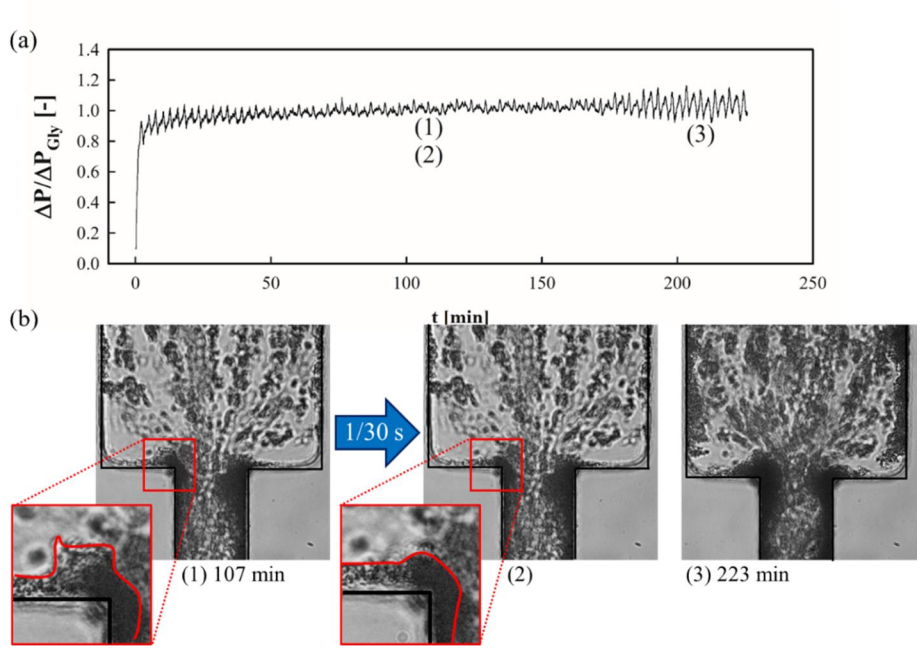

Fig. 4.4 (a) The normalized pressure drop of Gly70PS with time, and (b) the snapshots of the channel at the flow rate 1.0 ml/hr.

When the particles accumulated in the upstream, they affected the flow field too. The particle deposition acted as a blockage which obstructs the flow path. Fig. 4.5 shows the flow field of Gly60PS at 1.0 ml/hr after 88 min. The vortex, which was not observed in the beginning of the experiment, was formed on the left hand side of the upstream after about 80 min. As time proceeds, more particles piled up and the vortex grew larger in size (Fig. 4.5 (b)). The pressure drop also increased from 76.9 kPa at 88 min to 91.5 kPa at 94 min. The clogging structure was difficult to be identified precisely, but the structure of the clogging could be estimated locally. As shown in Fig. 4.5(b), the vortex was formed because the fluid could not pass through the contraction directly and bypassed. It can be conjectured that the particles next to the contraction throat (in the upstream) have accumulated enough to block the fluid to pass through. Therefore, the clogging can generate the formation of a vortex which does not exist in the flow of a Newtonian fluid. In Fig. 4.5(c), more particles were accumulated at the upstream and the pressure drop was increased to 116.6 kPa. Because the flow rate was 1.0 ml/hr, the average velocity at the upstream is $\overline{V_u} = Q/W_u h = 15.4\, mm/s$ (where $\overline{V_u}$ is the average velocity at the upstream). The flow velocity in the vortex was slow enough to track the particles. If it was fast, it appeared as a streak line, and the velocity at a specific location could not be calculated because the particle passed through the whole upstream part within 1 s. To calculated the velocity, the distance between the moving particles was measured by counting the number of pixels between the particles and converting it to the real dimension. The particles moved in the center of the vortex at 4.5 ~ 10.5

μm/s in 94 min, and at 2.2 ~ 4.5 μm/s in 118 min. The velocity inside the vortex was O(1~10 μm/s), which corresponds to about 1/1000 of the main stream velocity. It indicates that the residence time of the particles in this region can be longer than 1000 times than in the main stream. Therefore, clogging may form a dead space in which a material is confined for a long time during which the flow does not exchange materials with the main stream.

, ΔP = 116.6 kPa

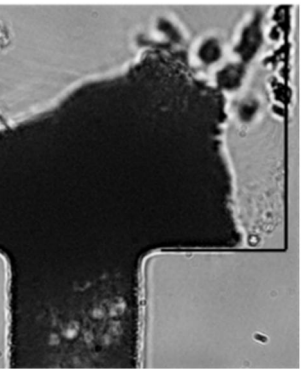

Fig. 4.5 Snapshots of Gly60PS at the flow rate of 1.0 ml/hr.

4.3 Effect of shear stress on pressure drop and clogging

Fig. 4.6(a) shows the pressure drop of Gly70PS. As time passed, the particles first deposited at the downstream, and they filled the downstream region. Thereafter, the area of the deposited particles extended out to the upstream. As the particles accumulated, the pressure drop increased, and the pressure drop decreased as the blockage of the channel was flushed out. Fig. 4.6(a) shows that the pressure drop fluctuated during the clogging process, and the increase in pressure drop seemed to be almost independent of the flow rate. For example, in Fig. 4.6(a), when the flow rate was 1.0 ml/hr, the pressure drop was maintained at about 90 kPa although the pressure drop at the flow rate 0.3 ml/hr was often larger than this value. When this pressure drop was normalized by the pressure drop at the same flow rate of the glycerol solution with no particle (Fig. 4.2(a)), the relationship between the flow rate and the pressure drop became more obvious (Fig. 4.6(b)). The x-axis of Fig 4.6(b) is the normalized time, which is the dimensionless number defined as the product of time and shear rate ($\dot{\gamma} = \frac{\overline{V_d}}{W_d/2} = \frac{Q}{hW_d^2/2}$) [11]. This dimensionless number means the total amount of the deformation for the fluid to experience inside the channel. When clogging occurred, the normalized pressure drop was larger than unity and showed peaks. On the other hand, when clogging did not occur, the normalized pressure drop hardly changed with time. That is, there exists no such a peak in the pressure drop.

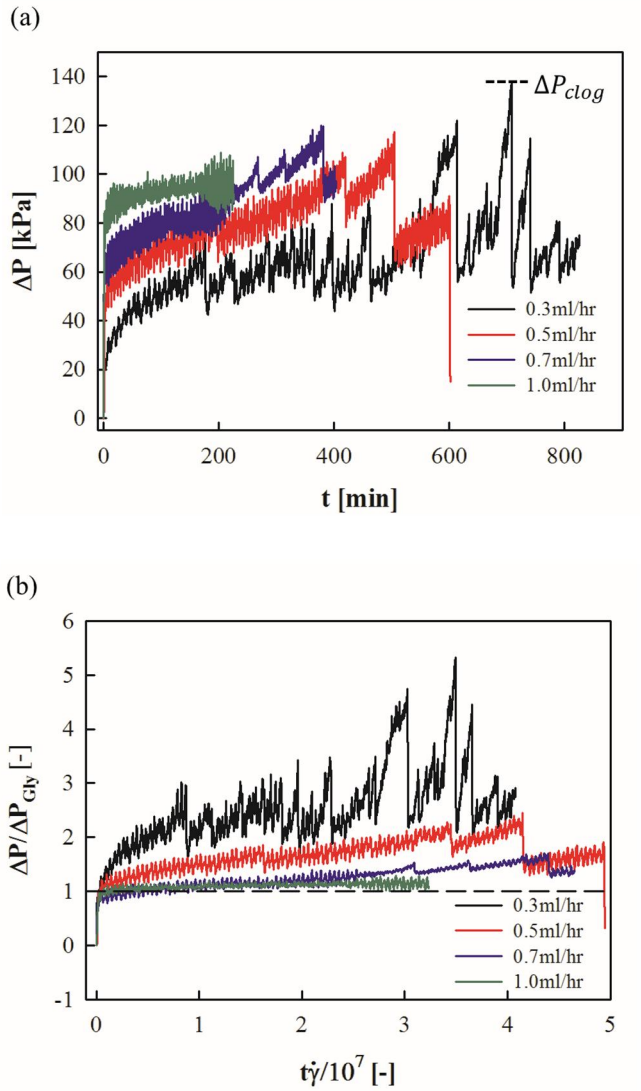

Fig. 4.6 (a) Differential pressure drop of Gly70 at various flow rates. (b) Normalized pressure drop versus normalized time.

To quantitatively analyze the effect of fluid viscosity on pressure drop, the highest pressure in each experiment was defined as the clogging pressure drop (ΔP_{clog}) at the specific flow rate. For example, in Fig. 4.6(a), the pressure drop showed a maximum at 137.6 kPa at the flow rate of 0.3 ml/hr in 707 min, which was the clogging pressure drop in this case. Also, the clogging pressure drop divided by the pressure drop without particles was defined as the normalized clogging pressure drop ($\Delta P_{clog}/\Delta P_{Gly}$). Unlike the clogging pressure drop which was difficult to find out any trend, the normalized clogging pressure drop shows a clear tendency. As shown in Fig. 4.7, for Gly60PS, the $\Delta P_{clog}/\Delta P_{Gly}$ rose up to as high as 13 at shear stress of 7.2 Pa (at flow rate of 0.3 ml/hr, see Table 1), which means that the pressure drop increased by 13 times as compared with the pressure drop of the Gly60. As the flow rate increased, the $\Delta P_{clog}/\Delta P_{Gly}$ decreased. For Gly70PS, the $\Delta P_{clog}/\Delta P_{Gly}$ was 5 at 14.8 Pa (at 0.3 ml/hr) and decreased to unity at 49.4 Pa (at 1.0ml/hr). For Gly80PS, $\Delta P_{clog}/\Delta P_{Gly}$ was already one at shear stress 58.5 Pa (at 0.5 ml/hr), that is, the clogging did not occur. The $\Delta P_{clog}/\Delta P_{Gly}$ decreased with the increase in fluid viscosity and flow velocity.

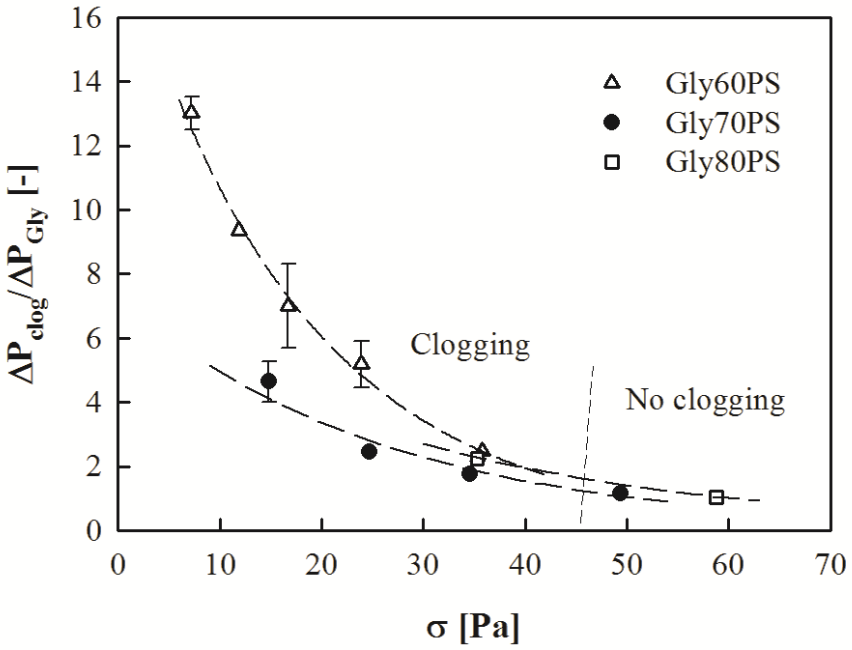

Fig. 4.7 Normalized clogging pressure versus shear stress of Gly60PS, Gly70PS and Gly80PS.

In Section 4.2, the "rolling" and "stick and detach" was observed, which implies that the accumulated particles are swept away by the flow. When the number of particles swept away (output) by the flow is smaller than that of the particles coming in (input), the amount of accumulated particles (accumulation) becomes large, leading to an intensive clogging. On the other hand, when the flow force is strong, it is hard for particles to get accumulated, in which case clogging is rarely observed [43]. Robert de Saint Vincent et al. reported negative aggregate growth rate, meaning that the deposited particles were swept out [46]. For high ionic strength, various aggregate shapes were formed depending on flow rate. Although the finger-shaped aggregate was built at a mild flow rate, the tip-shaped aggregate, which was of smaller size than the “finger”, was developed and the erosion of single particles at the extremity was observed, which agrees with our results. It was also reported that the clogging process was delayed as the flow rate increased, and it was explained that the increase in hydrodynamic force overcomes the repulsive forces for particle deposition and simultaneously breaks the interparticle and particle-wall bonding [47]. The particle detachment on a tilted-shape channel was also reported [38]. It is similar to the case in which the particles deposited on the body of aggregation are detached, leading to “stick and detach”. However, in these studies, there was no quantitive analysis about the hydrodynamic force.

The extent to which the fluid pushes the particles is related to the shear

stress. The glycerol solution used in this study is a Newtonian fluid whose viscosity does not change with the shear rate. The shear stress is expressed as the product of the fluid viscosity and the shear rate. That is, $\sigma = \eta\dot{\gamma}$, where σ is the stress and $\dot{\gamma}$ is the characteristic shear rate. Here, the characteristic shear rate is equal to the shear rate ($\dot{\gamma} = \frac{\overline{V_d}}{W_d/2} = \frac{Q}{hW_d^2/2}$) used in calculating the normalized time. Therefore, the shear stress of a Newtonian fluid is directly proportional to the flow rate and viscosity. That is, the higher the viscosity and flow rate, the larger the shear stress. Higher shear stress will prevent the particles being accumulated.

Table 4.1 shows the shear stress at each flow rate. For the case of Gly60PS, the shear stress was the lowest at the shear rate of 823 1/s (Q = 0.3 ml/hr). That is, the force pushing out the particles was not strong enough, which corresponds to a condition for the particles to be accumulated easily. As time passed, the particles continued to accumulate and the pressure drop increased at the same time. As the particles accumulated more, the flow path became narrower. Narrowing flow path significantly increases the shear rate, which is inversely proportional to the square of the downstream width, and it simultaneously increases the shear stress. As a result, the particles were swept away and the flow path was widened again. Accordingly, the shear rate decreased and the particles accumulated again. As the shear rate increased, the stress applied to the particles became larger and it was more difficult for the particles to be accumulated. As a result, the particles detached relatively easily and the normalized clogging

pressure increased less than that at low shear rate.

For the case of Gly80PS, when the shear rate was 1370 1/s (Q = 0.5 ml/hr), the clogging did not occur (Fig. 4.7). This is because the shear stress was already large enough to prevent the particles from accumulating. Since the particles did not accumulate much, the flow path did not become narrowed or deformed. Therefore, the clogging pressure drop did not change much due to the small change in shear rate. No clogging occurred at 2740 1/s (Q = 1.0 ml/hr) for Gly70PS. In ref. [46], the particles did not deposit at high shear rate regime, which corresponds to our result at high shear stress.

Fig. 4.7 shows the relationship between the normalized clogging pressure drop and shear stress. The normalized clogging pressure drop decreased exponentially with shear stress. It could be fitted in the exponential form, $\frac{\Delta P_{clog}}{\Delta P_{Gly}} = a \cdot e^{-b \cdot \sigma}$. The values of "b" were 0.057, 0.039, and 0.033 [1/Pa] for Gly60PS, Gly70PS, and Gly80PS, respectively. Above a certain shear stress (here, 50 Pa), no clogging occurred although it was observed at the lower stress regardless of fluid viscosity. This suggests that there might exist a critical stress level which prevents clogging. The critical stress is a function of the medium viscosity, the particle-particle and particle-wall interaction, and the kinematics in the flow geometry. In this study, the particle concentration, the type of the fluid, and the interaction between channel wall and particle were kept constant. As the Reynolds number was kept less than one, it can be said that the viscous force dominated the flow. In this case, when the stress is larger than a critical shear stress, the

particles rarely accumulate and form clogging.

Chapter 5.

Agglomerate breakup under extensional flow

5. Agglomerate breakup under extensional flow

5.1 Experimental

5.1.1 Materials

In this study, carboxyl poly (styrene) latex (PS, solid% = 4%, surface charge density = 2.9 μC / cm^2, Invitrogen, USA) with size of 0.1 μm was used. The particles were well-dispersed by electrostatic repulsion because they had negative charges on the surface. 1 M NaCl was used to form agglomerates [54, 57, 58, 60]. In this study, the viscosity of the medium as well as the flow rate was controlled to apply different stresses to the agglomerate. To prepare the samples, a calculated amount of NaCl was completely dissolved in deionized water, and then glycerol was mixed. Then, a pre-calculated amount of latex suspension was added. Since it can be difficult to observe a single agglomerate at high concentrations of particles, latex suspension was diluted in DI water for accuracy. The concentration of the particles used in this study was 200 and 400 ppm to form an appropriate number of agglomerates that were observed and studied. To control the viscosity, the concentrations of glycerol chosen were 60, 70, and 80 wt.%, and the viscosities were 5.0, 8.7, and 18.0 cp, respectively. For convenience, the samples were labelled as Gly50PS, Gly60PS, and Gly70PS according to their glycerol concentrations. The viscosity was measured

by using a rotational rheometer, DHR-3 (TA instruments, USA).

The morphology of the agglomerate depends on the process of agglomerate formation even with the same salt (i.e. the fractal dimension) [54, 57]. Harshe et. al. reported that the fractal dimension of the agglomerate formed in the stagnant diffusion-limited condition was 1.75 (open structure), whereas the value was 2.7 (dense structure) for the agglomerate in the stirred tank [54]. In this study, a sample was mixed using a magnetic stirrer to form agglomerates (mixing speed was 175 rpm). The samples were mixed for 48 hours for a full growth of the agglomerate. In order to characterize the morphology of the agglomerate formed, an approach to obtain the fractal dimension using the microscopy image of the agglomerate was used [77, 78]. In this method, the projected area, A, and the perimeter, P are measured to obtain the perimeter fractal dimension, dpf, from binary images of the agglomerates (the image process, which converts microscopy images into binary images, will be dealt with, in section 5.1.4). The relationship is as followed.

$$A \sim P^{2/d_{pf}} \quad (1)$$

To obtain the perimeter fractal dimension, the projected area and the perimeter of 100 agglomerates chosen randomly were measured. The perimeter fractal dimension, dpf = 1.44, was calculated by regression (see Fig. 5.1). The relationship between the fractal dimension, df and dpf, was df = -1.628dpf + 4.6 for 1.8 <df <2.4 [77] and df = -1.5dpf + 4.4 for 2.2 <df <3.0 [78]. The fractal dimension calculated by each

equation were approximately df = 2.25.

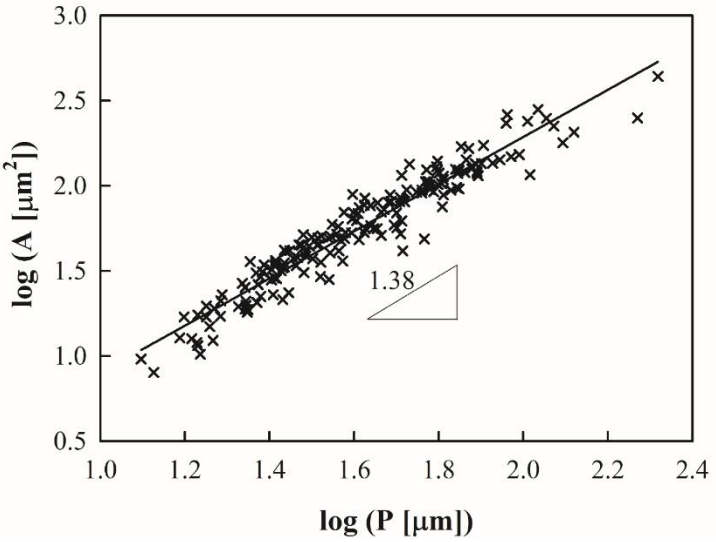

Fig. 5.1 The projected area versus the perimeter of the agglomerates. The slope from regression was 1.38.

5.1.2 Channel geometry

To apply a planar extensional flow to the agglomerate, a cross-shaped channel was employed (Fig. 5.2 (a)). As shown in Fig. 5.2(a, b), the fluids enter the channel through the upper and lower side, respectively, and meet at the cross region. Then, they exit to remaining two channels in the direction at a 90 degrees. The center of the cross region is called the stagnant point. To observe the breakup of agglomerates by extensional flow, the agglomerate must pass through the stagnant point. To do this, the agglomerate must be placed in the middle of the channel upstream. Otherwise, the agglomerate does not enter the stagnant point and does not experience extensional flow appropriately. Therefore, to focus on the agglomerates in the center, sheath flow is injected on both sides of the main flow, which carries the agglomerate (Sheath flow is a glycerol solution with the same viscosity to the main flow and with no particles). Thus, the channel is not a simple cross channel, but has a slightly more complex shape. In Fig. 5.2(a), the main flow is injected through inlet 1 and 2, and sheath flow is injected through inlet 3 and 4. The sheath flows come from the both sides of the main flow and meet the main flow (Fig. 5.2 (c)). There wasn't any notable instability occurring when sheath flow and main flow met for all experimental conditions. In addition, the agglomerate in the main flow did not

migrate to the sheath flow at all. As a result, the main flow and the sheath flow were appeared as laminar flow, and they did not mix with each other at all until the channel outlet.

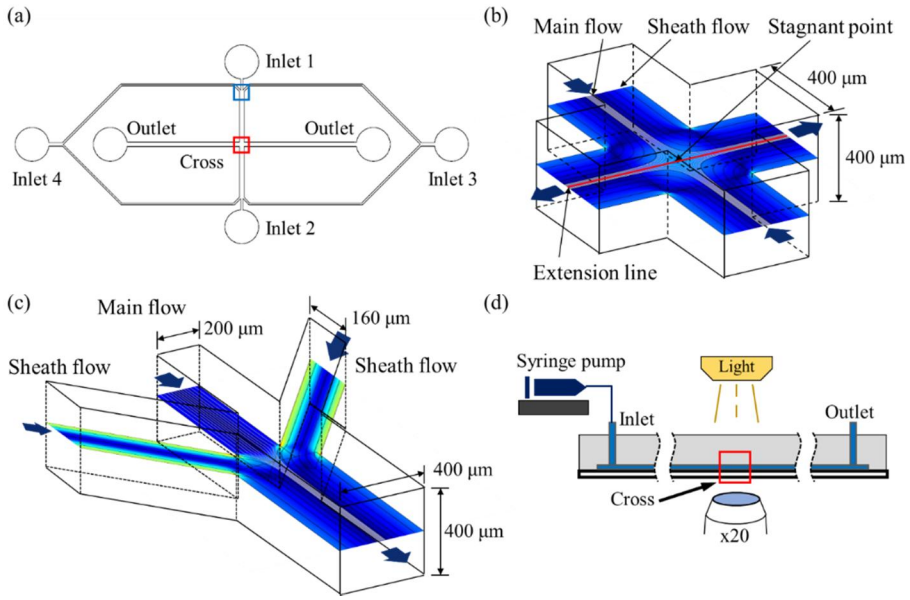

Fig. 5.2 (a) Top view of a channel. (b) Cross region. (c) Joint region. (d) Schematics of observation system.

5.1.3 Flow characterization

Before the experiment, COMSOL Multiphysics® Modeling Software (COMSOL Inc., U.S.A.) was used to set the experimental conditions and to figure out the shear rate and extensional rate of the flow field. 2D geometry including not only the cross region but also inlets and outlets was set. Fluid flow was set to laminar flow.

In order to examine the effect of sheath flow, the main flow was fixed at 1 ml/hr and the flow rate of the sheath flow was set to 1, 3, and 5 times of main flow. In Fig. 5.3, the gray line indicates the main flow and the black lines are for the sheath flows. As the sheath flows increased, the main flow area decreased. Therefore, to focus on the agglomerate at the stagnant point, the sheath flows should be increased. However, for stable operation, the flow rate of the sheath flow was fixed at 3 times of the main flow. The agglomerate near the stagnant point was deformed along the red line in Fig. 5.2(b). The flow field of the red line was examined with the increasing flow rates of the main flow from 1 to 3 ml/hr. The shear rate was almost zero and trivial (considering the linear channel, the shear rate of the channel is zero).

The extensional rate, on the other hand, was 97.3-291.0 1/s at the stagnant point (Fig. 5.4). As shown in Fig. 5.4, the extensional rate had a maximum value at the stagnant point (x=0) and it decreased away from the point. Therefore, the red line in Fig. 5.2(b) was defined as an extension line in this paper.

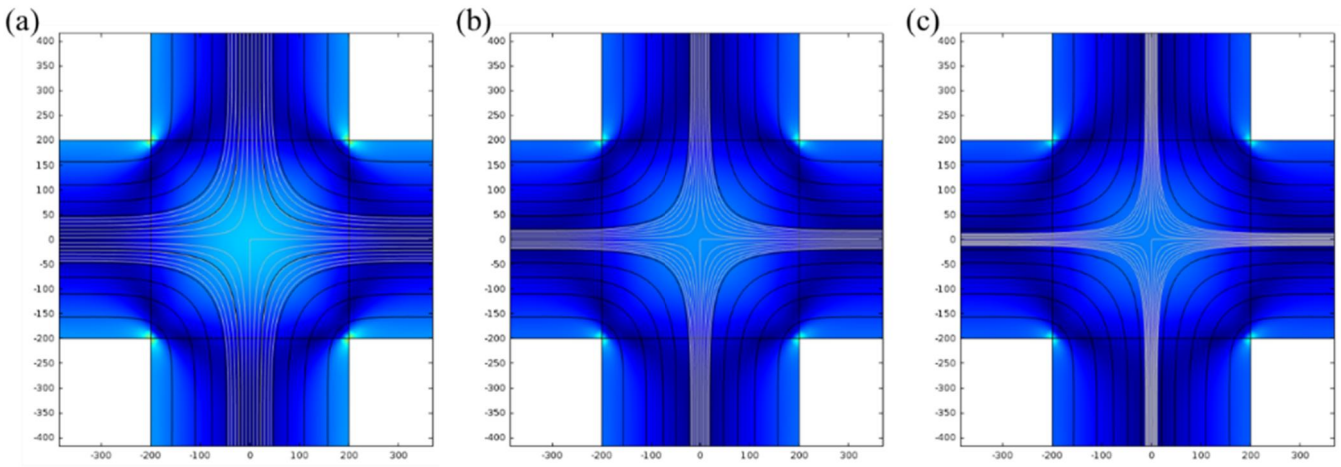

Fig. 5.3 Flow field according to the sheath flow when the main flow rate was 1.0 ml/hr. The sheath flows were (a) 1.0, (b) 3.0, and (c) 5.0 ml/hr.

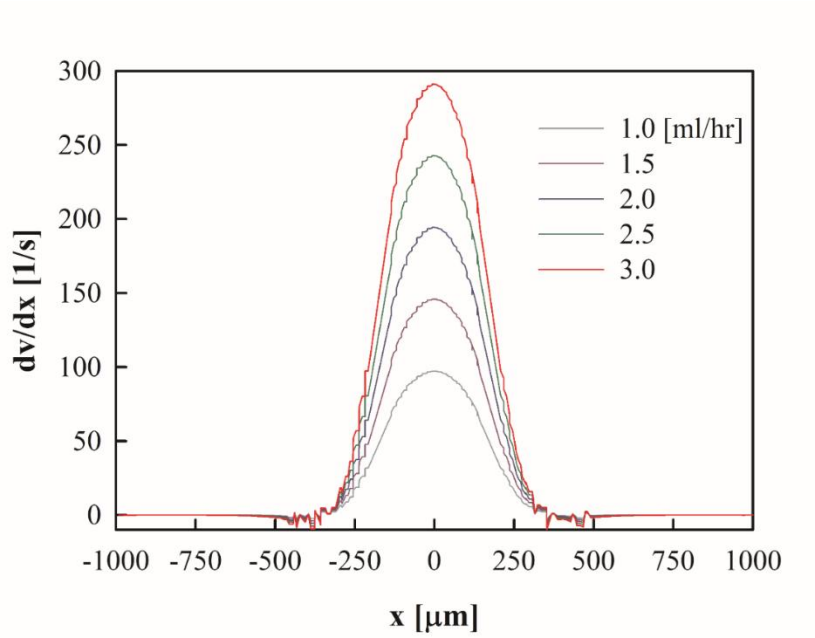

Fig. 5.4 Extensional rate with various main flow rate.

5.1.4 Image processing

The agglomerate stayed in the cross region for several tens to hundreds milliseconds. Agglomerate behavior was recorded using a high-speed camera. Since the frame rate was 2000 fps, about 200 images for a case were taken. To obtain the projected area and perimeter of the target agglomerate, these images were post-processed using a code of matlab (Mathwork, USA). In this code, the brightness intensities for each pixel of an arbitrary 70 images were read. That is, each pixel has 70 brightness values. The background of this case was generated by choosing the median value for each pixel (Fig. 5.5(b)). The background was removed from the images leaving only the moving agglomerates (Fig. 5.5(c)). Then, the images were sharpened and adjusted to make the shape of agglomerate more obvious (Fig. 5.5(d)). After that, the images were converted to binary images with a proper level of threshold (Fig. 5.5(e)). Finally, the number of pixels of the projected area and the perimeter of the target agglomerate was counted with Image J (https://imagej.nih.gov/ij/) and then converted to the real dimension.

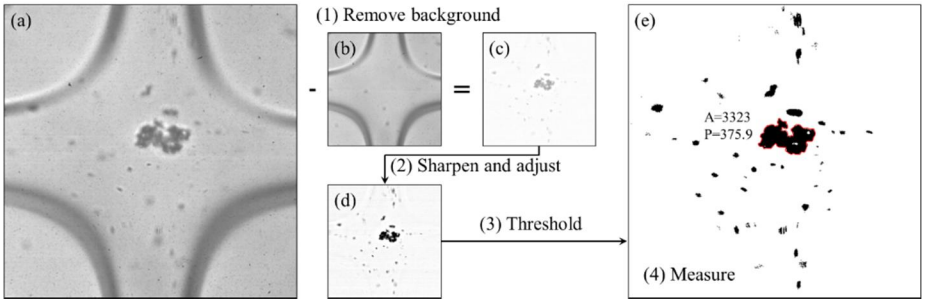

Fig. 5.5 Image process. (a) Original image. (b) Background image. (c) Image after removing the background. (d) Image after sharpening and adjusting. (e) Binary image. In the figure, the projected area and the perimeter of a target agglomerate were measure by using Image J.

5.2 Behavior of a single agglomerate

In the cross region, the agglomerate with various size could be observed. The average area of them was 432.5 μm^2 and the standard deviation was 406.0 μm^2. Agglomerates out of the center was excluded and the largest size of agglomerates was 2528.0 μm^2. Agglomerates out of the focus were also excluded.

In this section, first, the behaviors of a single agglomerate in the cross channel will be presented into two cases of a breakup and no breakup.

Fig. 5.6(a) shows the agglomerate passing through the channel without breakup. The glycerol concentration of the fluid used in this case was 50 wt.% and the main flow rate was 2.0 ml/hr. The moment when the agglomerate entered in the cross region (observation region) was arbitrarily set to 0 ms. As shown in Fig. 5.6(a), the agglomerate entered the cross region at 0.0 ms and reached the stagnant point at about 24.5 ms. After that, the agglomerate went to the left and completely exited the observation area at 52.5 ms. The projected areas of the agglomerate with time were measured by the images. The initial projected area of the agglomerate was about 644 μm^2 at 0 ms. The agglomerate was slightly stretched as it approached the stagnant point and the projected area increased to 736 μm^2 at the stagnant point. The area then increased to about 850 μm^2 when the agglomerate exited the observation area and it was 130% larger than the initial area. It was because the agglomerate was stretched as shown in Fig. 5.6(a). To quantify the behaviors of the

agglomerate, the agglomerate was fitted to the ellipse using Image J and a major axis and a minor axis were measured (See inset in Fig. 5.6(a)). Aspect ratio was defined as the ratio of the major axis to the minor axis. As shown in Fig. 5.6(c), the initial aspect ratio of agglomerate was about 1.7. This aspect ratio hardly increased until about 10 ms. After then, the aspect ratio of agglomerate began to increase. The time at which a portion of the agglomerate first reached the extension line was at 14.0 ms. From this moment, the aspect ratio increased to 2.7 until the agglomerate left the observation area. In other words, when the agglomerate reached the extension line, it was affected by the extensional flow and stretched. The angle between the long axis and the extension line was defined as the angle of agglomerate. The initial angle of the agglomerate was about 73 degrees. The agglomerate rotated while approaching the stagnant point and its value was 10 degree at 24.5 ms (at the stagnant point). In Fig. 5.6(a), the agglomerate was rotated up to where it was almost parallel to the extension line. The agglomerate then continued to rotate and left the observation region with the angle of 0 degrees.

It is noticed that among the cases for no breakup, this case is where the agglomerate was most stretched. In this case, the aspect ratio increased by about 1. However, for the most cases of no breakup, the aspect ratio increased by less than 1. In addition, in this case, the agglomerate rotated parallel to the observation plane, but some agglomerates were inverted at the stagnant point. In this case, the projected area either increased or decreased randomly.

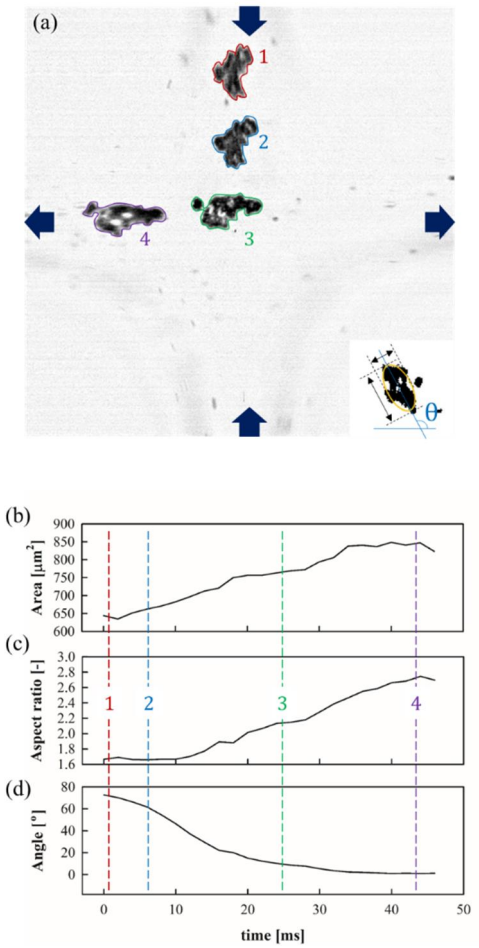

Fig. 5.6 Case for no breakup. The concentration of glycerol was 50 wt.% and the flow rate was 2.0 ml/hr. (a) Overlaid image. The agglomerate came into the cross region from upper side and left for the left. The numbers in figure indicate specific time at corresponding positions: 1 at 1.0, 2 at 6.5, 3 at 24.5, and 4 at 44 ms. (b) Projected area. (c) Aspect

ratio. (d) Angle with time.

Fig. 5.7 shows the case of that a single agglomerate was broken up at the stagnant point. The viscosity of glycerin was 70 wt.% and the flow rate was 1.5 ml/hr. Similarly to the previous case, the moment when the agglomerate entered the observation region was arbitrarily set to 0 ms. In Fig. 5.7(a)-1, the agglomerate entering the cross region was referred to 'a+b+c+d' because the agglomerate was finally broken into four fragments. The agglomerates experienced deformation and rotation while moving toward the stagnant point. The projected area, aspect ratio, and angle were also measured to quantify the behaviors of the agglomerate. It took about 20 ms until the agglomerate was located at the stagnant point from 0 ms when it entered the observation region. During this time, the projected area was maintained at approximately 530 μm^2, and the aspect ratio only increased by 0.8 from 2.0 to 2.8. However, the angle between the major axis and the extension line increased from 116 to 170 degrees, so the long axis was already almost parallel to the extension line. That is, agglomerate was not largely deformed but it was mainly rotated. The agglomerate then stayed at the stagnant point for about 12 ms and was stretched longer due to an extensional flow pulling on both sides of the agglomerate (Fig. 5.7(a)-2). As a result, the projected area increased to 638 μm^2 and aspect ratio increased by 3.9 to reach 6.7. On the other hand, the angle was increased by 10 degrees to 180 degrees. That is, at the stagnant point, deformation of agglomerate occurs mainly, which broke the

agglomerate. At 33 ms, the agglomerate could not withstand the extensional flow and was split into 'a' and 'b + c + d' fragments. After that, the fragment 'a' passed to the left of the channel. The fragment 'b + c + d' moving to the right was stretched continuously by the extensional flow, as the projected area increased. Then again at 36 ms, this was broken by the flow into two fragments ('b' and 'c + d' in Fig. 5.7(a)-4). Fragment 'b' was the nearest to the stagnant point and exited the observation area last (Fig. 5.7(b)). Fragment 'c + d' was again stretched by flow, and split into 'c' and 'd' at 46 ms after the projected area increased. It is noticeable that the agglomerate was initially broken at the stagnant point, but the subsequent two breakups occurred out of the stagnant point. As shown in Fig. 5.4, it is because the extensional rate is not zero outside the stagnant point but also exists. In Fig. 5.7(b), the area of the fragments did not change much, which means the final dispersed fragments were no longer deformed. The sizes of the smallest fragment 'd' and the largest fragment 'b' were about 140 μm^2 and 225 μm^2, respectively. This seems to be due to the fact that the flow at a given location was not enough to deform the fragments [65].

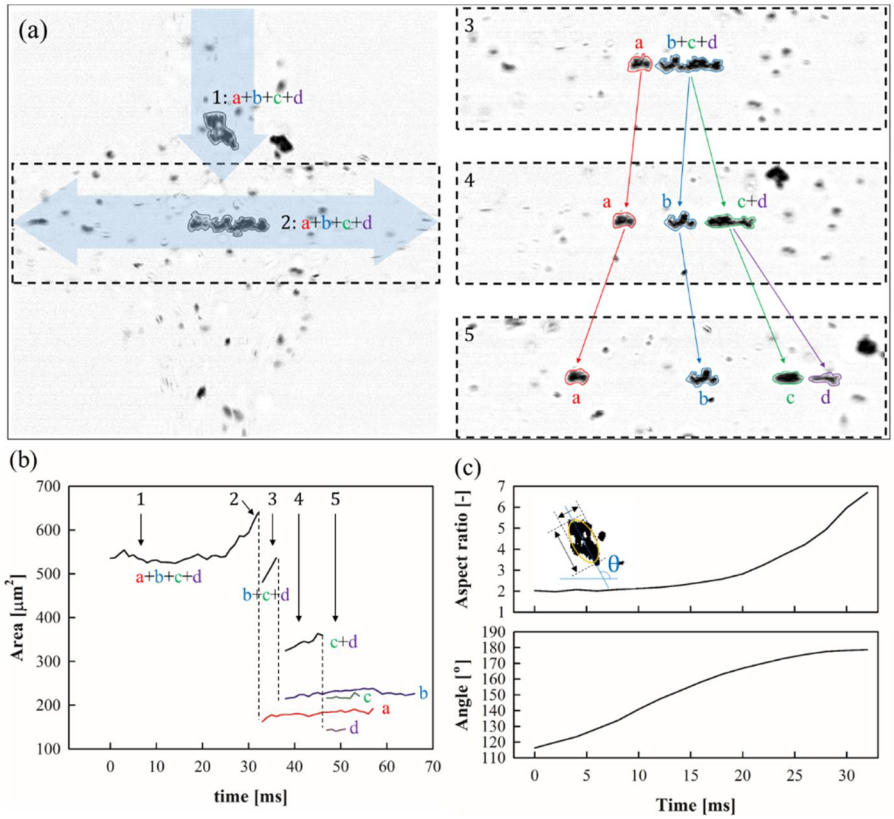

Fig. 5.7 Case for breakup. The concentration of glycerol was 70 wt.% and the main flow rate was 1.5 ml/hr. (a) Images for the process of agglomerate breakup: 1 at 5.5, 2 at 32, 3 at 34.5, 4 at 40, and 5 at 48 ms. (b) Projected area. The vertical dotted lines represent the time when the agglomerate was broken up. The breakup times were 33, 36, and 45 ms, respectively. (c) Aspect ratio and angle before the breakup.

5.3 Probability of agglomerate breakup

The faster the flow rate and the higher the viscosity of the fluid, the better the agglomerates were broken. However, the same flow condition did not mean that all agglomerates passing through the stagnant point were broken or not. In addition, even if the agglomerates of similar sizes passed the stagnant point in the same flow condition, the breakup of the agglomerates depended on the probability. The probability, p, is defined as the ratio of the number of broken agglomerates to that of the agglomerates passing through the stagnant point. Therefore, when all agglomerates are broken up, the probability is 1. On the contrary, all of the agglomerates are not broken, the value is zero. Approximately 50 (at least 40) agglomerates were observed for each flow conditions. As shown in Fig. 5.8, as both the flow rate and the viscosity increased, the probability of the breakup also increased. For Gly70PS, when the flow rate was 2.5 ml/hr, the probability of breakup was 0.92. On the other hand, for Gly50PS, when the flow rate was 1.5 ml/hr, the value was 0, which means any agglomerates that passed the stagnant point were not broken.

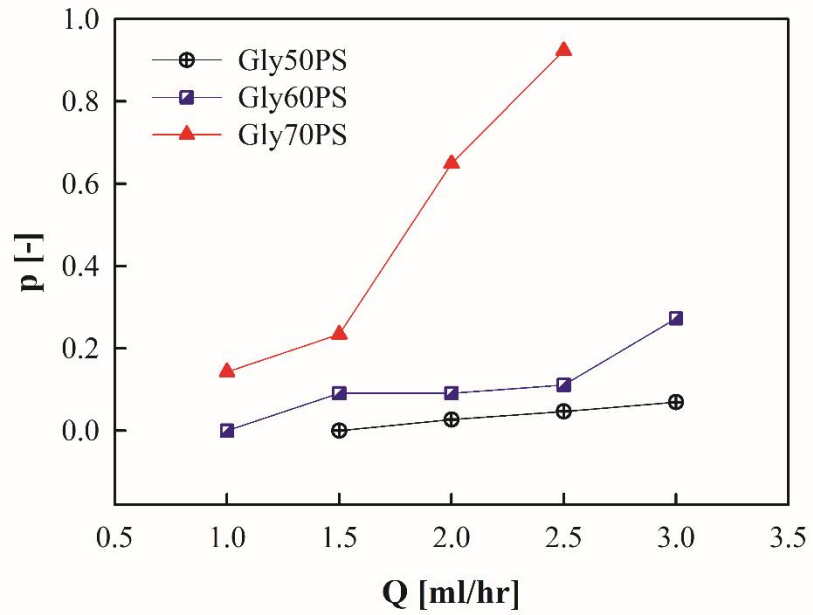

Fig. 5.8 Probability of breakup with the flow rate of samples.

5.4 Fragment distribution

In the previous section, it was shown that the agglomerates were broken up with a certain probability at given conditions. In this section, the distribution of fragments after breakup will be dealt with. The agglomerate, which was not broken, was treated as one fragment.

First, the size distribution of fragments was examined. The normalized fragment area, A_{frag} is defined as the ratio of the projected area of each fragment to the initial area of agglomerate before breakup. For a case, when the initial area of agglomerate was 1070 μm^2 and it was split into three fragments of 177, 309, and 781 μm^2, so that the normalized fragment areas were 0.17, 0.29, and 0.73, respectively. Here, since the sum of the area of the fragments is larger than the initial area, it could be appeared to be strange. However, as mentioned earlier, because agglomerates are stretched with the increasing projected area, the sum of the projected areas of all fragments is usually larger than the initial area of the agglomerate. Thus, for the cases of breakup, the sum of the normalized fragment areas is usually larger than one. Conversely, when an agglomerate passes through the stagnant point without breakup, the normalized fragment area becomes the ratio of the projected area before the agglomerate leave the observation region to the initial area. In this case, the value was randomly either larger or smaller than 1 depending on the rotation at the stagnant point. The normalized

fragment area of all fragments was acquired from the same data used to obtain the probability of breakup. The interval of the normalized fragment area was divided and the fraction, f was defined as the ratio of the number of fragments in the corresponding interval to the total number of fragments to examine the distribution of the normalized fragment area according to each flow condition. The normalized fragment area was divided by an interval of 0.2. For an example, when the flow rate was 2.5 ml/hr for Gly70PS, the number of fragments corresponding to $0 \leq A_{frag} \leq 0.2$ was 69, 45 for $0.2 \leq A_{frag} \leq 0.4$, 21 for $0.4 \leq A_{frag} \leq 0.6$, 16 for $0.6 \leq A_{frag} \leq 0.8$, 4 for $0.8 \leq A_{frag} \leq 1.0$, 2 for $1.0 \leq A_{frag} \leq 1.2$, and 1 for $1.2 \leq A_{frag} \leq 1.4$. The total number of all fragments was 158. Therefore, the fractions of each interval were 0.44, 0.28, 0.13, 0.10, 0.025, 0.013, and 0.006. Also, for this flow condition, the fragments, of which the areas have 10% of the initial area of the agglomerates, occupied 44%. Thus, the distribution of the normalized fragment area shows quantitatively how much agglomerates are split into fragments with a certain size. Likewise, the fragment distribution functions were calculated for other flow conditions (Fig. 5.9).

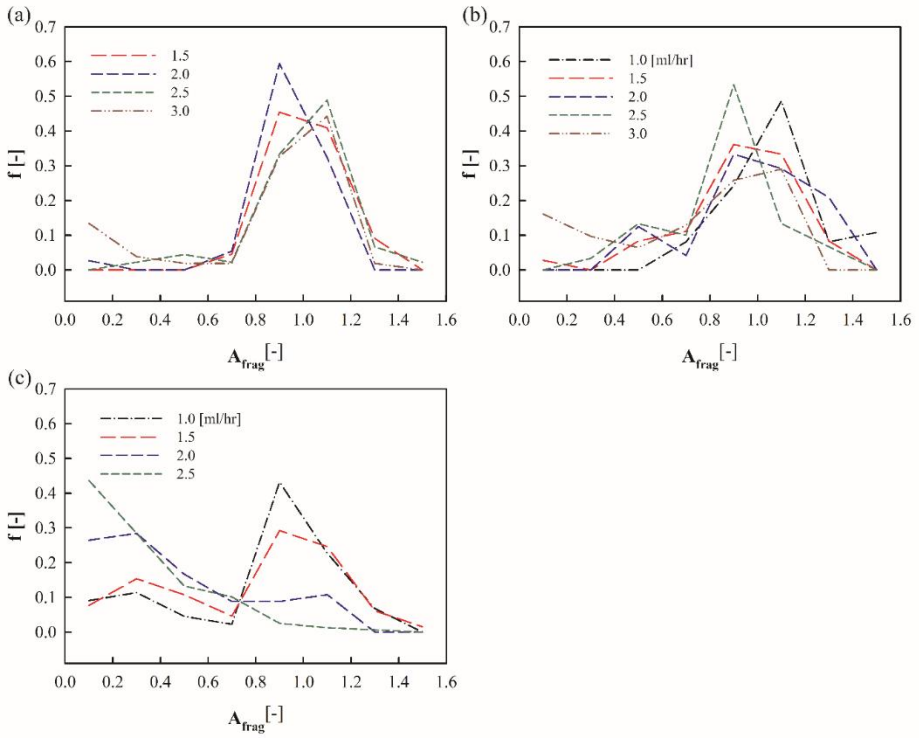

Fig. 5.9 Fragment distribution of (a) Gly50PS, (b) Gly60PS, and (c) Gly70PS.

For readability, Fig. 5.10(a) shows the fragment distribution of Gly70PS with flow rate of only 1.0 and 2.5 ml/hr. For flow rate of 1.0 ml/hr, the fraction with the normalized fragment area of 0.9 ($0.8 \leq A_{frag} \leq 1.0$) was 0.43 and the largest. The probability of breakup at this flow rate was 0.14 (Fig. 5.8), which means that a small amount of agglomerates was broken up. For this case, the change in the projected area is due to the rotation of the agglomerate around the stagnant point. Therefore, the normalized fragment area had a value close to 1 mainly. On the other hand, for the flow rate of 2.5 ml/hr, the fraction with the normalized fragment area of 0.1 ($0 \leq A_{frag} \leq 0.2$) was the largest at 0.44. For this flow conditions, the probability was 0.92 (Fig. 5.8), and most agglomerates were broken up. Hence, the normalized fragment area had a smaller value than one. Likewise, for other flow conditions, the normalized fragment area decreases with the increasing flow rate.

Fig. 5.10(b) shows the mean fragment area, $\bar{A}_{frag}$, for each flow condition. This is the average of all normalized fragment areas for each condition, which means how large an agglomerate is split into fragments under a given flow field. For an example, for a Gly70PS with a flow rate of 2.5 ml/hr, the mean fragment area is about 0.31 (it is roughly calculated to be 0.30 from above data because the representative of the interval is used as the normalized fragment area.). The error bar in the graph represents one standard deviation, which

means an approximate fragment distribution. For Gly50PS and Gly60PS, the mean fragment areas are close to 1 for low flow rates. It is because the flow condition is not sufficient to break the agglomerate so that the agglomerate is not broke and simply rotates at the stagnant point. On the other hand, for Gly70PS, the mean fragment area is about 0.82 even for the flow rate of 1.0 ml/hr, and it decreased to 0.31 as the flow rate increased. Therefore, as the viscosity and the flow rate increase, the agglomerates are dispersed into the smaller fragments.

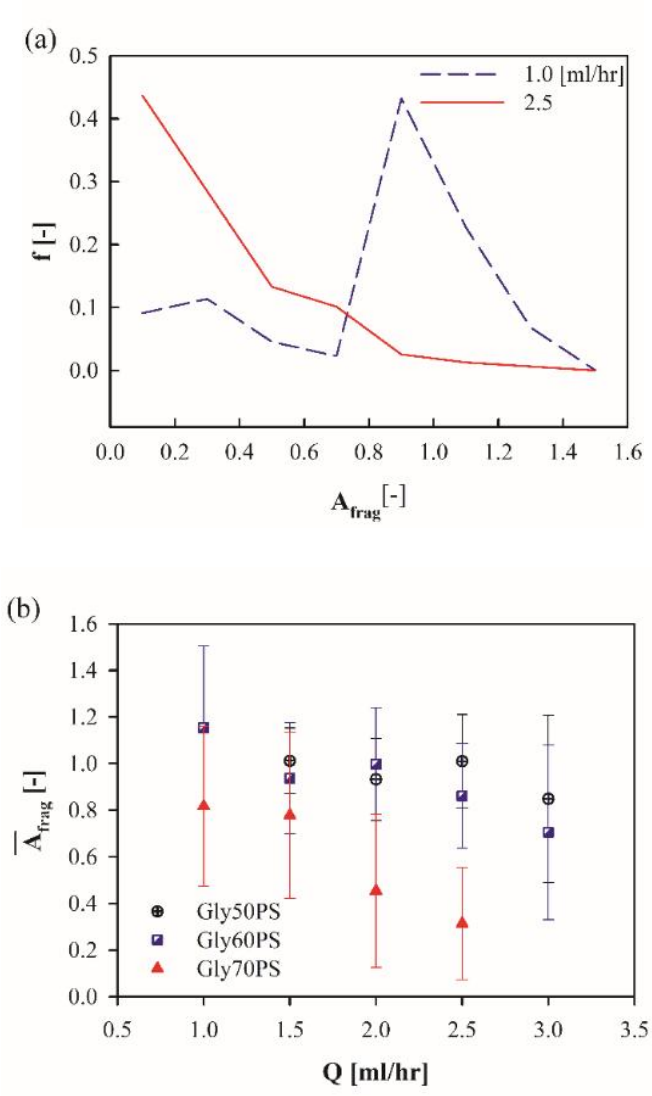

Fig. 5.10 (a) Fragment distribution of Gly70PS with the flow rate of 1.0

and 2.5 ml/hr. (b) Average fragment fraction of samples for flow conditions.

It was also examined how many fragments an agglomerate is divided into. When the projected area and the perimeter of agglomerates and fragments were measured, the number of fragments, nfrag was also counted at the same time. When the initial area of the agglomerate is 1070 μm^2, and it is split into three fragments of 177, 309, and 781 μm^2 (the example mentioned above), the number of fragments, n_{frag} is 3. Also, for no breakup cases, the number of fragments is 1. For each flow condition, the number of fragments, n_{frag} was counted and divided by the total number of agglomerates to obtain the fraction of each number of fragments. For an example, for Gly70PS with a flow rate of 2.5 ml/hr, the total number of agglomerates observed was 40. In this case, since the number of non-breakup cases is 3, the fraction with the number of fragment of 1 becomes 3/40 = 0.075 (Fig. 5.11(c)). On the other hand, since the number of agglomerates divided into three fragments was 11, the fraction with the number of fragment of 3 was 11/40 = 0.275 (Fig. 5.11(c)). In this way, the distribution of number of fragments was obtained for each flow condition (Fig. 5.11).

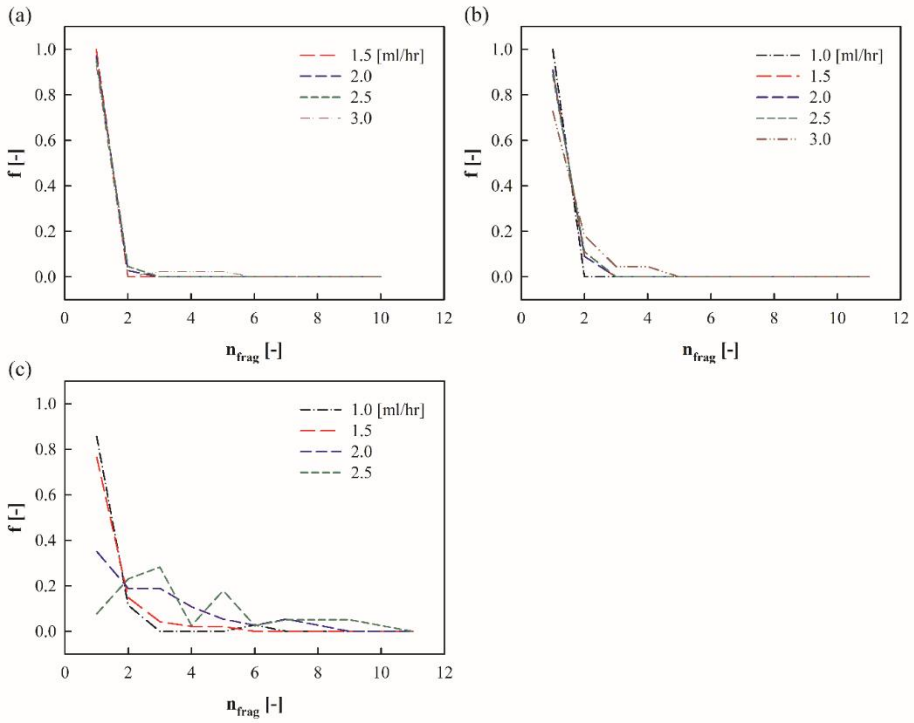

Fig. 5.11 Number of fragments of (a) Gly50PS, (b) Gly60PS, and (c) Gly70PS.

For convenience, Fig. 5.12(a) shows the distribution of number of fragments of Gly70PS for flow rate of only 1.0 and 2.5 ml/hr. At low flow rate (1.0 ml/hr), the fractions were 0.86, 0.11, and 0.03 for the number of fragment of 1, 2, and 6, respectively. This means that most of the agglomerates were not broken up, and this result matches the fact that the fraction with the normalized fragment area of about 1 was the largest. On the other hand, when the flow rate was high (2.5 ml/hr), the fraction for the number of fragment of 1 was only 0.075. The fraction with the number of fragment of 3 was the largest at 0.275. There was the case in which one agglomerate was divided into 10 fragments. However, for Gly50PS and Gly60PS, most agglomerates were not broken due to low viscosity and the fraction with the number of fraction of 1 was largest.

Fig. 5.12(b) shows the average number of fragments, $\bar{n}_{frag}$, which is the average value of all of the number of fragment and shows how many fragments an agglomerate is split into. For an example, for Gly70PS with the flow rate of 2.5 ml/hr, it was about 4.3, meaning that one agglomerate was divided into 4.3 fragments on average. The error bar in the graph represents one standard deviation, indicating the approximate distribution of the number of fragments of an agglomerate fragment. In Fig. 5.12(b), the mean numbers of fragment of Gly50PS and Gly60PS have values of 1 for most flow rates and 1.2 and 1.4 for 3.0 ml/hr, respectively. This means that the flow was not strong enough

to break the agglomerate. On the other hand, for Gly70PS, the mean number of fragment increased to 4.3 for the flow rate of 2.5 ml/hr while it was 1.3 when the flow rate was 1.0 ml/hr.

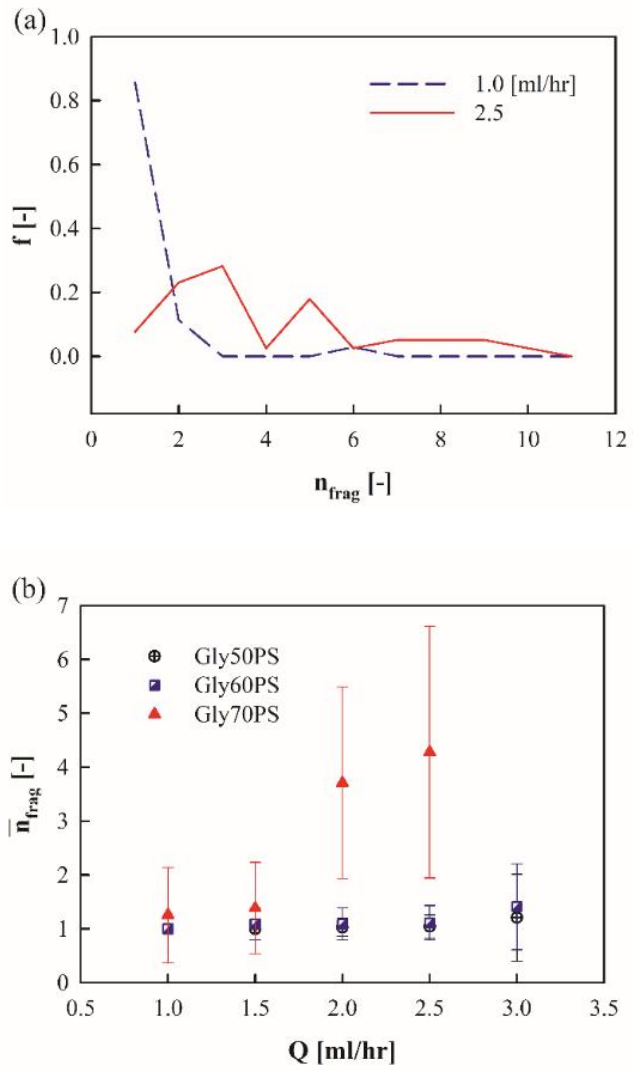

Fig. 5.12 (a) Number of fragments of Gly70PS with the flow rate of 1.0 and 2.5 ml/hr. (b) Average number of fragments of samples for flow

conditions.

5.5 Master curves

From the probability of breakup, p, the mean fragment area, $\bar{A}_{frag}$, and the mean number of fragment, $\bar{n}_{frag}$, the agglomerates could be divided into smaller and more fragments well as the viscosity and the flow rate increased, which means the stress increased. To calculate the stress applied to the agglomerates, the planar extensional viscosity of the Newtonian fluid, which is four times the shear viscosity [79], is used. Since the breakup of the agglomerate that passed the stagnant point was observed, the extensional rate, which was calculated at the stagnant point from COMSOL, was used as mentioned in section 2.3. Thus, the largest stress, which the agglomerate could experience for each flow condition, was used.

Fig. 5.13(a) shows the probability of breakup with the stress calculated. Although fluid viscosities and flow rate were different, the probabilities for each condition are superimposed on a master curve. In other words, the probability of agglomerate breakup is a function of the applied stress. At the lowest stress of 2.9 Pa in this experiment, no agglomerate was broken (p = 0). On the other hand, at the highest stress of 17.5 Pa, the probability of breakup was 0.92. The dashed line in the graph is the result of fitting the data to the s-shaped curve as shown below:

$$\mathrm{p} = \frac{a}{1+e^{\frac{-(\sigma-\sigma_{0.5})}{b}}} \tag{2}$$

Here, when the stress increases infinitely, the probability become one, so that a equals one. $\sigma_{0.5}$ and b are fitting parameters and 12.6 and 2.3 Pa, respectively. $\sigma_{0.5}$ is the stress when the probability of breakup is 0.5 and the inflection point of s-shape curve.

The mean fragment area, $\bar{A}_{frag}$ and the mean number of fragment, $\bar{n}_{frag}$ also well agreed with a master curve (Fig. 5.13(b, c)). Fig. 5.13(b) shows the mean fragment area with the applied stresses. For low stress, the mean fragment area was about 1, which means that most agglomerates were no broken. However, it decreased above a critical stress and the slop was about -0.06. The critical stress obtained by fitting was about 6.1 Pa and the probability calculated by equation (2) at 6.1 Pa is 0.06. Fig. 5.13(c) shows the mean number of fragment with stresses. For low stress, it was about one, which indicates no breakup occurred. On the other hand, for high stress, the mean number of fragment increased and it had similar shape curve with the probability of breakup.

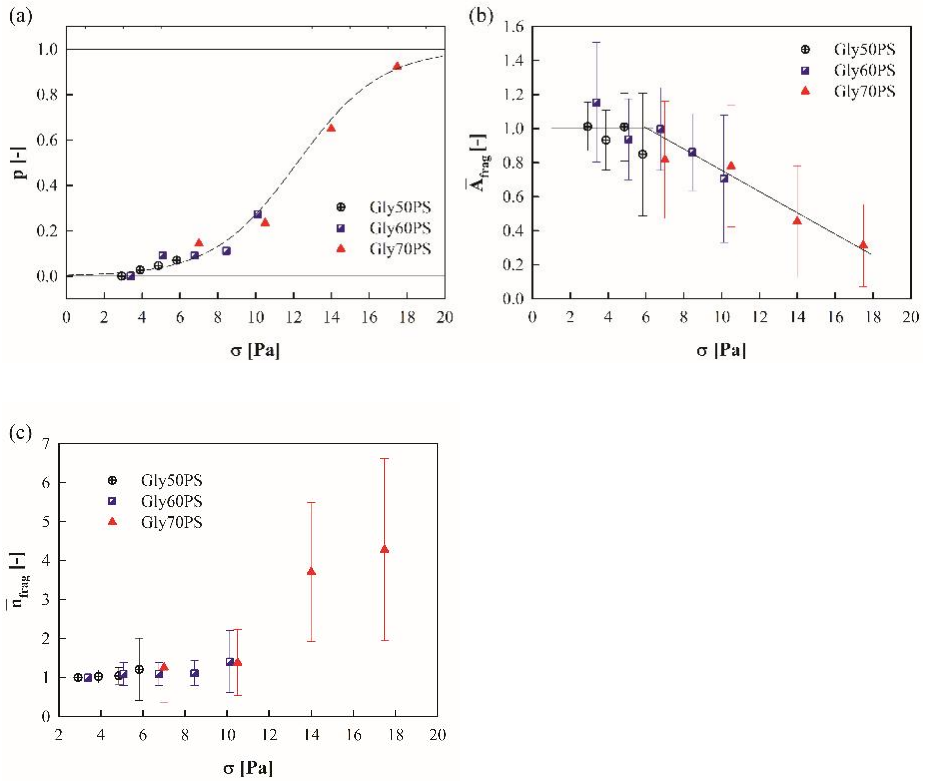

Fig. 5.13 (a) Probability of breakup, (b) mean fragment area, and (c) mean number of fragment with stress.

5.6 Model prediction

In a previous study, a steady aggregation size of agglomerates with high fractal dimension (d_f=2.4-3.0) was obtained by 100 passes through a mixed flow of both shear and extensional flow [60]. The radius of gyration, Rg, followed the scaling law of $R_g \sim \sigma^{-1/5(d-d_f)} \sim \sigma^q$ with stress [60]. Here, $q = -1/5(d - d_f)$ and d=3. In addition, for 2.2 <d_f <3, the number of primary particles, N, has the following relationship with given A and P [78]:

$$N \sim \left(\frac{A^2}{P}\right)^{0.9} = \left(\frac{A^2}{A^{d_{pf}/2}}\right)^{0.9} = A^{0.9(2-d_{pf}/2)} \quad (3)$$

Therefore, the following relationship holds in this system (d_{pf}=1.44, d_f=2.25).

$$A \sim N^{1/0.9(2-d_{pf}/2)} \sim \left(R_g^{d_f}\right)^{1/0.9(2-d_{pf}/2)} \sim \sigma^{qd_f/0.9(2-d_{pf}/2)} \sim \sigma^{-0.52} \quad (4)$$

To confirm this, the relationship between the stress and the mean projected area of fragments was examined. Fig. 5.14 is a plot of log A versus log σ above the critical stress. The dotted line in the figure is a linear regression with a slope of -0.55, which is in good agreement with the exponent, -0.52 in the scaling law. In previous studies, the aggregation had to pass the nozzle 100 times to have a steady state size. However, in this study, the breakup of agglomerates was occurred by a strong extensional flow only once.

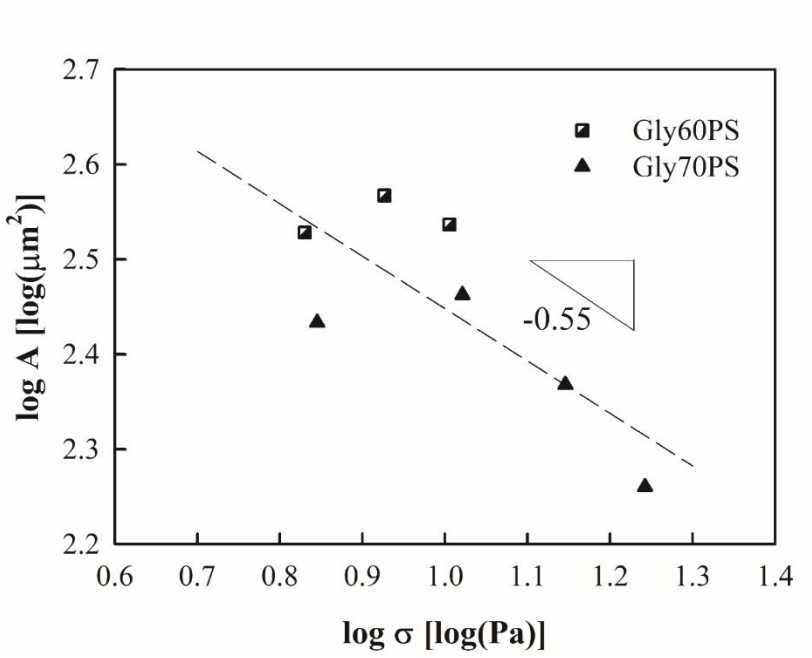

Fig. 5.14 Mean projected area of fragments versus stress.

Chapter 6. Summary

6. Summary

In this thesis, the dynamics of particulate suspensions in complex flow including vortex formation, channel clogging, and agglomerate breakup was studied.

First, the effect of silica particles on both the rheological properties and the vortex behavior in a micro-contraction channel was investigated through comparisons with PEO solutions and silica/PEO suspensions. The flow of the PEO solutions without silica developed in the sequence of a Newtonian-like flow, a lip vortex, and then a corner vortex with the increase in the flow rate. The flow rate at which the lip vortex or corner vortex formed was dependent upon the fluid properties. The higher the viscoelasticity, the larger the vortex size. To ascertain the effect of silica particles, the PEO concentration was fixed at 1.0 wt% and the silica concentration was varied from 1.0 to 8.0 wt%. Like the PEO solutions, the vortex of the silica/PEO suspension developed with an increase in the flow rate, and the sequence was identical. However, the silica particles influenced the size of the vortex and the flow rate at which the lip or corner vortex formed. The vortex size did not increase monotonously; rather, the size decreased initially and then started to increase with an increase in the silica concentration. Both the viscosity and storage modulus decreased and then increased with an increase in

the silica concentration. However, the fluid elasticity influenced the vortex behaviors more significantly than the viscosity. The observation that both the vortex size and storage modulus decreased and then increased with an increase in the silica concentration could be explained by the adsorption of polymer onto the silica particles. When the silica particles were added to the PEO solution, some of the polymers in the medium were adsorbed onto the surface of the silica particles. Consequently, some of the free polymer in the medium was used, i.e., as much as 45% of the initial amount. The decrease in the amount of free polymer resulted in a significant decrease in the storage modulus despite the fact that only 1.0wt% of silica was added. However, the total amount of adsorption rarely varied with an increase in the silica concentration because the amount of adsorption per unit area decreased. The same tendency was observed when the suspension was compensated with additional polymers corresponding to the amount of adsorbed polymer. Therefore, the change in the storage modulus due to polymer adsorption affected the size of the vortex and the flow rate at which the lip or corner vortex formed.

Second, the clogging mechanism of PS particles dispersed in glycerol solutions during the contraction flow was investigated. The concentration of PS particles was fixed at 0.05 wt. %, and the channel with an upstream width of 180 μm and a contraction ratio of four was used. The process that small particles, which were much smaller than the size of the channel (the smallest length scale of the channel was 45 μm and the particle size was about 0.5 μm), accumulated and finally clogged the channel in the single pore was examined. The particles

deposited first in the downstream. In this process, the "rolling" behavior, in which the approaching particles were stuck temporarily and rolled over by the flow, was observed. It is important in determining whether the particles would continue to accumulate or not. In addition to "rolling", another interesting behavior, “stick and detach” was observed. This indicates that no matter how well the particles are dispersed in the fluid, a large agglomerate can be formed when the clogging process is not managed properly. When the particles accumulated enough in the downstream region, the clogging structure expanded to the upstream. This extended structure had a significant effect on the flow in the channel. The clogging structure interfered with the passage of the fluid, which resulted in the formation of the vortex. Newtonian fluid hardly generates vortex at low Reynolds number in the micro contraction channel, but the vortex formation by clogging could be easily observed. This is important because the vortex or the dead space can cause unpredicted stay of the particles during the process. The pressure increased as the particles accumulated, and the pressure decreased as the particles swept away. The effect of fluid viscosity on the clogging behavior was also investigated. To quantitatively compare this, the point at which the maximum pressure drop was defined as the clogging pressure drop. The normalized clogging pressure drop was defined as the clogging pressure drop divided by the pressure drop when there was no particle. At low flow rate and viscosity, the pressure drop was significantly increased over time, resulting in a very large normalized clogging pressure drop (for Gly60PS, it increased to 13 at 0.3 ml/hr). However, for Gly80PS, the clogging did not occur and the normalized

clogging pressure drop was only unity even at the flow rate of 0.5 ml/hr. To investigate the relationship between the clogging and the flow conditions, the stress of the fluid was calculated. The normalized clogging pressure drop decreased exponentially with shear stress. When the stress was small, it was difficult to remove the particles. They easily accumulated and the pressure drop increased significantly. However, when the stress was large, the particles were easily washed away, and the normalized clogging pressure drop was reduced. When this stress was very large, the channel was rarely clogged for a long time. Therefore, there exists a critical stress that determines whether the clogging will build up or not.

Lastly, the breakup process of the aggregation under the planar extensional flow was observed and quantitatively analyzed. Poly(styrene) particles and salt were used to form the agglomerates, and glycerol was used to control the stress level of the fluid. To characterize the morphology of the agglomerates formed by mild mixing, the projected area and perimeter of the aggregation were measured from the microscopic images. The fractal dimension of the agglomerate calculated using the perimeter fractal dimension, which is obtained by the relationship between the projected area and the perimeter, was 2.25. The cross channel was employed to apply the planar extensional flow. The agglomerate of the main flow was focused toward the stagnant point by sheath flows. The agglomerate mainly rotated approaching the stagnant point and the major axis of the agglomerate aligned parallel to the extension line. At the stagnant point, the aggregation was pulled by the flow and was stretched, resulting in

the increase of aspect ratio. The probability of breakup was dependent upon the applied stress, and the probability increased with a sigmoidal curve according to the increasing stress. At low stress, the probability of breakup was low, and the aggregation was mainly rotated with little stretching at the stagnant point. Thus, the mean fragment area was almost one and the mean number of fragment was also one. On the other hand, above the critical stress, it was split into several fragments, and the mean fragment area was smaller than one and decreased with a slope of -0.06 with the increase in stress. Besides, the number of fragments was increased with the applied stress. The probability of breakup and the size and number distribution functions are a function of an applied stress, and they well agree with master curves according to the stress. In addition, the mean area of the fragments showed a power-law relationship with the applied stress. The exponent was -0.55, which was in good agreement with the scaling law.

References

1. M.A. Alves, P.J. Oliveira, F.T. Pinho, Benchmark solutions for the flow of Oldroyd-B and PTT fluids in planar contractions. Journal of Non-Newtonian Fluid Mechanics, 2003. 110(1): p. 45-75.
2. D.V. Boger, Viscoealstic flows through contractions. Ann. Rev. Fluid Mech., 1987. 19: p. 157-182.
3. Y. Kwon, Numerical description of elastic flow instability and its dependence on liquid viscoelasticity in planar contraction. Journal of Rheology, 2012. 56(6): p. 1335.
4. G.H. McKinley, W.P. Raiford, R.A. Brown, R.C. Armstrong, Nonlinear dynamics of viscoelastic flow in axisymmetric abrupt contractions. Journal of Fluid Mechanics, 1991. 223: p. 411-456.
5. S. Nigen, K. Walters, Viscoelastic contraction flows: comparison of axisymmetric and planar configurations. Journal of Non-Newtonian Fluid Mechanics, 2002. 102(2): p. 343-359.
6. J.P. Rothstein, G.H. McKinley, Extensional flow of a polystyrene Boger fluid through a 4 : 1 : 4 axisymmetric

contraction/expansion. Journal of Non-Newtonian Fluid Mechanics, 1999. 86(1–2): p. 61-88.

7. B. Yesilata, A. Öztekin, S. Neti, Instabilities in viscoelastic flow through an axisymmetric sudden contraction. Journal of Non-Newtonian Fluid Mechanics, 1999. 85(1): p. 35-62.
8. M.A. Alves, R.J. Poole, Divergent flow in contractions. Journal of Non-Newtonian Fluid Mechanics, 2007. 144(2-3): p. 140-148.
9. L.E. Rodd, J.J. Cooper-White, D.V. Boger, G.H. McKinley, Role of the elasticity number in the entry flow of dilute polymer solutions in micro-fabricated contraction geometries. Journal of Non-Newtonian Fluid Mechanics, 2007. 143(2-3): p. 170-191.
10. D. Lee, K.H. Ahn, Flow patterns in 4:1 micro-contraction flows of viscoelastic fluids. Korea-Australia Rheology Journal, 2015. 27(2): p. 65-73.
11. L.E. Rodd, T.P. Scott, D.V. Boger, J.J. Cooper-White, G.H. McKinley, The inertio-elastic planar entry flow of low-viscosity elastic fluids in micro-fabricated geometries. Journal of Non-Newtonian Fluid Mechanics, 2005. 129(1): p. 1-22.
12. L.E. Rodd, D. Lee, K.H. Ahn, J.J. Cooper-White, The importance of downstream events in microfluidic viscoelastic entry flows: Consequences of increasing the constriction length. Journal of Non-Newtonian Fluid Mechanics, 2010. 165(19-20): p. 1189-1203.
13. M.N. Oliveira, M.A. Alves, F.T. Pinho, G.H. McKinley, Viscous flow through microfabricated hyperbolic contractions.

Experiments in Fluids, 2007. 43(2-3): p. 437-451.

14. L. Campo-Deaño, F.J. Galindo-Rosales, F.T. Pinho, M.A. Alves, M.N. Oliveira, Flow of low viscosity Boger fluids through a microfluidic hyperbolic contraction. Journal of Non-Newtonian Fluid Mechanics, 2011. 166(21-22): p. 1286-1296.
15. D. Lee, Y. Kim, K. Ahn, Effect of elasticity number and aspect ratio on the vortex dynamics in 4:1 micro-contraction channel flow. Korea-Australia Rheology Journal, 2014. 26(3): p. 335-340.
16. W. Han, K.H. Ahn, In situ flow visualization of capillary flow of concentrated alumina suspensions. Rheologica Acta, 2013. 52(6): p. 547-556.
17. W. Han, K. Ahn, Pressure-driven flows of concentrated alumina suspensions depending on dispersion states of particles. Rheologica Acta, 2014. 53(3): p. 209-218.
18. B. Kirby, Micro- and nanoscale fluid mechanics : transport in microfluidic devices. 2010: Cambridge University Press.
19. S. Mathur, B.M. Moudgil, Adsorption Mechanism(s) of Poly(Ethylene Oxide) on Oxide Surfaces. Journal of Colloid and Interface Science, 1997. 196(1): p. 92-98.
20. J. Rubio, J.A. Kitchener, The mechanism of adsorption of poly(ethylene oxide) flocculant on silica. Journal of Colloid and Interface Science, 1976. 57(1): p. 132-142.
21. A.A. Zaman, M. Bjelopavlic, B.M. Moudgil, Effect of Adsorbed Polyethylene Oxide on the Rheology of Colloidal Silica Suspensions. Journal of Colloid and Interface Science, 2000.

226(2): p. 290-298.

22. A.A. Zaman, Effects of Polymer Bridging and Electrostatics on the Rheological Behavior of Aqueous Colloidal Dispersions. Particle & Particle Systems Characterization, 2003. 20(5): p. 342-350.

23. A.A. Zaman, B.M. Moudgil, Role of electrostatic repulsion on the viscosity of bidisperse silica suspensions. Journal of Colloid and Interface Science, 1999. 212(1): p. 167-175.

24. A.A. Zaman, R. Tsuchiya, and B.M. Moudgil, Adsorption of a Low-Molecular-Weight Polyacrylic Acid on Silica, Alumina, and Kaolin. Journal of Colloid and Interface Science, 2002. 256(1): p. 73-78.

25. R. Joksimovic, S. Prévost, R. Schweins, M.S. Appavou, M. Gradzielski, Interactions of silica nanoparticles with poly(ethylene oxide) and poly(acrylic acid): Effect of the polymer molecular weight and of the surface charge. Journal of Colloid and Interface Science, 2013. 394(0): p. 85-93.

26. H, Liu, H. Xiao, Adsorption of poly(ethylene oxide) with different molecular weights on the surface of silica nanoparticles and the suspension stability. Materials Letters, 2008. 62(6–7): p. 870-873.

27. B. Dersoir, M. de Saint Vincent, M. Abkarian, H. Tabuteau, Clogging of a single pore by colloidal particles. Microfluidics and Nanofluidics, 2015. 19(4): p. 953-961.

28. H. M. Wyss, D. L. Blair, J. F. Morris, H. A. Stone, D. A. Weitz, Mechanism for clogging of microchannels. Physical Review E,

2006. 74(6): p. 061402.

29. Y. Kim, K.H. Ahn, S.J. Lee, Effect of silica particles on vortex dynamics in a micro-contraction channel flow of poly(ethylene oxide) solutions. Journal of Non-Newtonian Fluid Mechanics, 2016. 234: p. 170-177.

30. D. Choi, S. Jung, Y. Won, J. H. Jang, J. Lee, H. Chae, K. Ahn, S. Lee, P. Park, C. Lee, Three-dimensional hydraulic modeling of particle deposition on the patterned isopore membrane in crossflow microfiltration. Journal of Membrane Science, 2015. 492: p. 156-163.

31. S. Jung, Y. Won, J. H. Jang, J. H. Yoo, K. Ahn, C. Lee, Particle deposition on the patterned membrane surface: Simulation and experiments. Desalination, 2015. 370: p. 17-24.

32. Y. Won, S. Jung, J. H. Jang, J. Lee, H. Chae, D. Choi, K. Ahn, C. Lee, P. Park, Correlation of membrane fouling with topography of patterned membranes for water treatment. Journal of Membrane Science, 2016. 498: p. 14-19.

33. N. Shafaei, M. Jahanshahi, M. Peyravi, Q. Najafpour, Self-cleaning behavior of nanocomposite membrane induced by photocatalytic WO3 nanoparticles for landfill leachate treatment. Korean Journal of Chemical Engineering, 2016. 33(10): p. 2968-2981.

34. G. C. Agbangla, É. Climent, P. Bacchin, Experimental investigation of pore clogging by microparticles: Evidence for a critical flux density of particle yielding arches and deposits. Separation and Purification Technology, 2012. 101: p. 42-48.

35. P. Bacchin, Q. Derekx, D. Veyret, K. Glucina, P. Moulin, Clogging of microporous channels networks: role of connectivity and tortuosity. Microfluidics and Nanofluidics, 2014. 17(1): p. 85-96.
36. E. Dressaire, A. Sauret, Clogging of microfluidic systems. Soft Matter, 2017. 13(1): p. 37-48.
37. Y. Kim, K.H. Ahn, S.J. Lee, Clogging mechanism of poly(styrene) particles in the flow through a single micro-pore. Journal of Membrane Science, 2017. 534: p. 25-32.
38. T. van de Laar, S. ten Klooster, K. Schroen, J. Sparkel, Transition-state theory predicts clogging at the microscale. Scientific Reports, 2016. 6: p. 28450.
39. A. Sauret, E.C. Barney, A. Perro, E. Villermaux, H.A. Stone, E. Dressaire, Clogging by sieving in microchannels: Application to the detection of contaminants in colloidal suspensions. Applied Physics Letters, 2014. 105(7): p. 074101.
40. M. Schoenitz, L. Grundemann, W. Augustin, S. Scholl, Fouling in microstructured devices: a review. Chemical Communications, 2015. 51(39): p. 8213-8228.
41. V. Ramachandran, H.S. Fogler, Plugging by hydrodynamic bridging during flow of stable colloidal particles within cylindrical pores. Journal of Fluid Mechanics, 1999. 385: p. 129-156.
42. P. Bacchin, P. Aimar, R.W. Field, Critical and sustainable fluxes: Theory, experiments and applications. Journal of Membrane Science, 2006. 281(1–2): p. 42-69.

43. G. Brans, A. van Dinther, B. Odum, C.G.P.H. Schroën, R. M. Boom, Transmission and fractionation of micro-sized particle suspensions. Journal of Membrane Science, 2007. 290(1–2): p. 230-240.
44. P. Bacchin, A. Marty, P. Duru, M. Meireles, P. Aimar, Colloidal surface interactions and membrane fouling: Investigations at pore scale. Advances in Colloid and Interface Science, 2011. 164(1–2): p. 2-11.
45. Z.A. Kuznar, M. Elimelech, Direct microscopic observation of particle deposition in porous media: Role of the secondary energy minimum. Colloids and Surfaces A: Physicochemical and Engineering Aspects, 2007. 294(1–3): p. 156-162.
46. M. Robert de Saint Vincent, M. Abkarian, H. Tabuteau, Dynamics of colloid accumulation under flow over porous obstacles. Soft Matter, 2016. 12(4): p. 1041-1050.
47. Z.B. Sendekie, P. Bacchin, Colloidal Jamming Dynamics in Microchannel Bottlenecks. Langmuir, 2016. 32(6): p. 1478-1488.
48. R.C. Sonntag, W.B. Russel, Structure and breakup of flocs subjected to fluid stresses. Journal of Colloid and Interface Science, 1986. 113(2): p. 399-413.
49. R.C. Sonntag, W.B. Russel, Structure and breakup of flocs subjected to fluid stresses. Journal of Colloid and Interface Science, 1987. 115(2): p. 390-395.
50. Y.M. Harshe, M. Lattuada, Breakage Rate of Colloidal Aggregates in Shear Flow through Stokesian Dynamics.

Langmuir, 2012. 28(1): p. 283-292.

51. J. Lee, S. Sung, Y. Kim, J.D. Park, K.H. Ahn, A new paradigm of materials processing—heterogeneity control. Current Opinion in Chemical Engineering, 2017. 16: p. 16-22.

52. M.U. BÄBler, M. Morbidelli, J. BaŁDyga, Modelling the breakup of solid aggregates in turbulent flows. Journal of Fluid Mechanics, 2008. 612: p. 261-289.

53. J.H. Choi, Y.W. Nam, J.S. Hong, Microfluidic study on CNT dispersion during breakup of aqueous alginic acid drop in continuous PDMS phase. Korea-Australia Rheology Journal, 2013. 25(1): p. 1-8.

54. Y.M. Harshe, M. Lattuada, M. Soos, Experimental and Modeling Study of Breakage and Restructuring of Open and Dense Colloidal Aggregates. Langmuir, 2011. 27(10): p. 5739-5752.

55. K. Higashitani, K. Iimura, H. Sanda, Simulation of deformation and breakup of large aggregates in flows of viscous fluids. Chemical Engineering Science, 2001. 56(9): p. 2927-2938.

56. S. Kim, J. Xu, A. Biswas, J.L. Willett, Shear-induced aggregate formation in starch solutions. Carbohydrate Polymers, 2006. 64(2): p. 168-174.

57. D. Saha, M. Soos, B. Lüthi, M. Holzner, A. Liberzon, M.U. Bäbler, W. Kinzelbach, Experimental Characterization of Breakage Rate of Colloidal Aggregates in Axisymmetric Extensional Flow. Langmuir, 2014. 30(48): p. 14385-14395.

58. M. Soos, L. Ehrl, M.U. Bäbler, M. Morbidelli, Aggregate

Breakup in a Contracting Nozzle. Langmuir, 2010. 26(1): p. 10-18.

59. M. Soos, A.S. Moussa, L. Ehrl, J. Sefcik, H. Wu, M. Morbidelli, Effect of shear rate on aggregate size and morphology investigated under turbulent conditions in stirred tank. Journal of Colloid and Interface Science, 2008. 319(2): p. 577-589.

60. A. Zaccone, M. Soos, M. Lattuada, H. Wu, M.U. Bäbler, M. Morbidelli, Breakup of dense colloidal aggregates under hydrodynamic stresses. Physical Review E, 2009. 79(6): p. 061401.

61. P.J. Lu, J.C. Conrad, H.M. Wyss, A.B. Schofield, D.A. Weitz, Fluids of Clusters in Attractive Colloids. Physical Review Letters, 2006. 96(2): p. 028306.

62. S. Blaser, Flocs in Shear and Strain Flows. Journal of Colloid and Interface Science, 2000. 225(2): p. 273-284.

63. Park, J.D., K.H. Ahn, N.J. Wagner, Structure-rheology relationship for a homogeneous colloidal gel under shear startup. Journal of Rheology, 2017. 61(1): p. 117-137.

64. G.H. McKinley, Visco-Elasto-Capillary Thinning and Break-Up of Complex Fluids. Ann. Rheol. Rev., 2005: p. 1-48.

65. P.R. Start, S.D. Hudson, E.K. Hobbie, K.B. Migler, Breakup of carbon nanotube flocs in microfluidic traps. Journal of Colloid and Interface Science, 2006. 297(2): p. 631-636.

66. J.C. McDonald, D.C. Duffy, J.R. Anderson, D.T. Chiu, H. Wu, O.A. Schueller, G.M. Whitesides, Fabrication of microfluidic systems in poly(dimethylsiloxane). Electrophoresis, 2000. 21(1):

p. 27-40.

67. J.M.K. Ng, I. Gitilin, A.D. Stroock, G.M. Whitesides, Components for integrated poly(dimethylsiloxane) microfluidic systems. Electrophoresis, 2002. 23(20): p. 3461-3473.

68. S. Bhattacharya, Y. Gao, V. Korampally, M.T. Othman, S.A. Grant, K. Gangopadhyay, S. Gangopadhyay, Mechanics of plasma exposed spin-on-glass (SOG) and polydimethyl siloxane (PDMS) surfaces and their impact on bond strength. Applied Surface Science, 2007. 253(9): p. 4220-4225.

69. W. Stöber, A. Fink, E. Bohn, Controlled growth of monodisperse silica spheres in the micron size range. Journal of Colloid and Interface Science, 1968. 26(1): p. 62-69.

70. G. Xu, J. Zhang, G. Song, Effect of complexation on the zeta potential of silica powder. Powder Technology, 2003. 134(3): p. 218-222.

71. L.E. Rodd, T.P. Scott, J.J. Cooper-White, G.H. McKinley, Capillary break-up rheometry of low-viscosity elastic fluids. Applied Rheology, 2005. 15(1): p. 12-27.

72. W.W. Graessley, Polymer chain dimensions and the dependence of viscoelastic properties on concentration, molecular weight and solvent power. Polymer, 1980. 21(3): p. 258-262.

73. V. Tirtaatmadja, G.H. McKinley, J.J. Cooper-White, Drop formation and breakup of low viscosity elastic fluids: Effects of molecular weight and concentration. Physics of Fluids, 2006. 18(4): p. 043101.

74. T. Saigal, J.K. Riley, P.L. Golas, R. Bodvik, P.M. Claesson, K.

Matyjaszewski, R.D. Tilton, Poly(Ethylene Oxide) Star Polymer Adsorption at the Silica/Aqueous Interface and Displacement by Linear Poly(Ethylene Oxide). Langmuir, 2013. 29(12): p. 3999-4007.

75. M.H. Kang, S.J. Lee, Rheological and electrical properties of polystyrene/multi-walled carbon nanotube nanocomposites prepared by latex technology. Korea-Australia Rheology Journal, 2012. 24(2): p. 97-103.

76. J. Kestin, M. Sokolov, W. Wakeham, Theory of capillary viscometers. Applied Scientific Research, 1973. 27(1): p. 241-264.

77. C. Lee, T.A. Kramer, Prediction of three-dimensional fractal dimensions using the two-dimensional properties of fractal aggregates. Advances in Colloid and Interface Science, 2004. 112(1): p. 49-57.

78. L. Ehrl, M. Soos, M. Lattuada, Generation and Geometrical Analysis of Dense Clusters with Variable Fractal Dimension. The Journal of Physical Chemistry B, 2009. 113(31): p. 10587-10599.

79. C.J.S. Petrie, Extensional viscosity: A critical discussion. Journal of Non-Newtonian Fluid Mechanics, 2006. 137(1): p. 15-23.

국문 초록

본 논문에서는 복잡 유동장에서 발생하는 입자 현탁액의 거동 중 와류 형성과 유로 막힘 그리고 응집체 분산에 대해 연구하였다. 이 학위 논문은 세 가지 목적이 있다.

첫번째로 수축형 미세 유로 내에서 실리카 입자가 poly(ethylene) oxide (PEO)용액의 와류 거동에 미치는 영향에 대해서 규명하였다. 산업적으로 사용되는 많은 재료들은 단순히 고분자 용액이나 멜트 뿐만 아니라 고분자와 입자를 포함하고 있는 현탁액이다. 하지만, 고분자와 입자 간의 상호작용이 유동장에 미치는 영향에 관한 연구는 거의 전무하다. 이 논문에서는 PEO 용액과 실리카/PEO 용액의 물성과 거동을 비교함으

로써 유동에 미치는 실리카 입자의 영향을 살펴보았다. 1.0 wt.%의 실리카 입자의 첨가는 와류 크기의 감소를 야기하였으며 lip vortex의 형성과 corner vortex로의 발달을 지연시켰다. 그리고 실리카의 농도가 증가함에 따라서, 와류 크기가 증가할 뿐만 아니라, lip vortex와 corner vortex를 형성하는 유속이 감소하였다. 이러한 수축형 미세 유로 내 와류 거동은 유체의 점성보다는 탄성에 기인하였다. 유체의 탄성을 대표하는 저장탄성률(storage modulus) 역시 와류 거동과 마찬가지로 실리카의 농도에 따라서 감소한 후 증가하였다. 와류 크기와 저장탄성율의 감소는 입자 표면으로의 고분자 흡착에 기인하였다. 1.0 wt.%의 실리카 입자가 첨가되었을 때, 매질 내에 존재하는 자유 고분자 (free polymer) 의 함량이 감소하기 때문에 저장탄성률이 감소하였다. 그 후, 고분자의 흡착량은 일정하게 유지되는 반면, 입자의 함량이 증가하면서 저장탄성률은 증가하였다. 흡착된 고분자의 함량만큼 고분자 함량을 보상해주었을 때, 탄성이 회복되어 와류의 크기 역시 회복되는 모습을 보였다.

두번째로, 한 개의 미세 유로 내에서 poly(styrene) 입자의 막힘 과정에 대해서 연구하였다. 이 연구에서는 현미경을 통한 관찰뿐만 아니라 압력 강하를 실측하였다. 압력은 유로 내 쌓인 입자의 양에 영향을 받았다. 유로 막힘 과정 동안 입자는 유체의 흐름에 의해서 떨어져 나가기도 하였는데, “rolling”과 “stick and detach” 과정이 완전히 유로를 막을 것인지 말 것인지를 결정하는 중요한 요소였다. 일정한 유속 이상에는 유로가 막히지

않았으며 압력이 증가하지 않았다. 유로의 상단부에 쌓인 입자들은 유체의 흐름에도 영향을 주었다. 이 경우, 흐름은 쌓인 입자에 의해서 우회하였으며 이로 인해 와류가 형성되었다. 유속과 유체의 점도가 높을수록 입자가 경험하는 유체의 스트레스가 커지며 이로 인해 입자가 유로에 쌓이기 힘들었다. 스트레스가 충분히 클 때, 입자는 유체의 흐름을 이기지 못하고 유로 막힘 현상은 저지되었다.

마지막으로 십자 형태 유로 내에서 순수한 평면 신장 유동을 경험하는 poly(styrene) 입자 응집체의 변형과 분산을 정량적으로 분석하였다. 불안정화된 poly(styrene) 입자에 전단 유동을 가함으로써 응집체를 형성하였으며 응집체의 형태를 대변하는 fractal dimension은 2.25였다. 십자 유로의 한 가운데인 정체점 (stagnant point) 에 응집체를 집중시키기 위해서 본 흐름 (main flow) 양쪽에 외 흐름 (sheath flow)를 가해 주었다. 응집체는 정체점에 도달하기 전에는 주로 회전을 하였으며, 정체점에서는 평면 신장 유동장에 의해서 길쭉하게 늘어나다가 분산되었다. 하지만 같은 흐름 조건에서 비슷한 크기의 응집체가 신장 유동을 경험하더라도 무조건 응집체가 분산되거나 그렇지 않는 것은 아니었다. 주어진 흐름 조건에 대해서 일정한 확률에 의해서 응집체는 분산되었다. 분산 확률과 파편 분산 (fragment distribution)은 유속과 점도에 의존하였으며, 스트레스에 따른 하나의 마스터 곡선 (master curve) 위에 중첩되었다. 또한, 가해주는 스트레스가 증가할수록 파편의 크기는 일정한 멱함수

(power-law) 관계를 가지고 감소하였으며 이 때 지수는 모델링의 결과와 잘 일치하였다.

본 연구를 통해 고분자와 입자간의 상호작용이 유변 물성 및 유동장에 어떻게 영향을 미치는 지에 대한 이해를 바탕으로 다양한 입자계 현탁액의 디자인과 공정 설계가 가능할 것으로 기대된다. 또한, 유동장 내에서 일어나는 응집체 형성과 분산에 대한 메커니즘을 이해함으로써 공정에 필요한 응집체의 크기를 조절하는데 기여할 수 있을 것으로 기대한다.

주요어: 입자계 현탁액, 흡착, 와류, 유로 막힘 과정, 응집, 응집체, 분산

학 번: 2013-30280